

RESEARCH ARTICLE

Nanomedicine-mediated recovery of antioxidant glutathione peroxidase activity after oxidative-stress cellular damage: Insights for neurological long COVID

Thelma Akanchise¹ | Borislav Angelov² | Angelina Angelova¹ 

¹Université Paris-Saclay, CNRS, Institut Galien
Paris-Saclay, Orsay, France

²Extreme Light Infrastructure ERIC,
Department of Structural Dynamics, Dolni
Brezany, Czech Republic

Correspondence

Angelina Angelova, Université Paris-Saclay,
CNRS, Institut Galien
Paris-Saclay, F-91400 Orsay, France.
Email: angelina.angelova@universite-paris-saclay.fr

Funding information

European Regional Development Fund;
European Commission

Abstract

Nanomedicine for treating post-viral infectious disease syndrome is at an emerging stage. Despite promising results from preclinical studies on conventional antioxidants, their clinical translation as a therapy for treating post-COVID conditions remains challenging. The limitations are due to their low bioavailability, instability, limited transport to the target tissues, and short half-life, requiring frequent and high doses. Activating the immune system during coronavirus (SARS-CoV-2) infection can lead to increased production of reactive oxygen species (ROS), depleted antioxidant reserve, and finally, oxidative stress and neuroinflammation. To tackle this problem, we developed an antioxidant nanotherapy based on lipid (vesicular and cubosomal types) nanoparticles (LNPs) co-encapsulating ginkgolide B and quercetin. The antioxidant-loaded nanocarriers were prepared by a self-assembly method via hydration of a lyophilized mixed thin lipid film. We evaluated the LNPs in a new in vitro model for studying neuronal dysfunction caused by oxidative stress in coronavirus infection. We examined the key downstream signaling pathways that are triggered in response to potassium persulfate (KPS) causing oxidative stress-mediated neurotoxicity. Treatment of neuronally-derived cells (SH-SY5Y) with KPS (50 mM) for 30 min markedly increased mitochondrial dysfunction while depleting the levels of both glutathione peroxidase (GSH-Px) and tyrosine hydroxylase (TH). This led to the sequential activation of apoptotic and necrotic cell death processes, which corroborates with the crucial implication of the two proteins (GSH-Px and TH) in the long-COVID syndrome. Nanomedicine-mediated treatment with ginkgolide B-loaded cubosomes and vesicular LNPs showed minimal cytotoxicity and completely attenuated the KPS-induced cell death process, decreasing apoptosis from 32.6% (KPS) to 19.0% (MO-GB), 12.8% (MO-GB-Quer), 14.8% (DMPC-PEG-GB), and 23.6% (DMPC-PEG-GB-Quer) via free radical scavenging and replenished GSH-Px levels. These findings indicated that GB-LNPs-based nanomedicines may protect against KPS-induced apoptosis by regulating intracellular redox homeostasis.

This is an open access article under the terms of the [Creative Commons Attribution-NonCommercial](https://creativecommons.org/licenses/by-nc/4.0/) License, which permits use, distribution and reproduction in any medium, provided the original work is properly cited and is not used for commercial purposes.

© 2024 The Author(s). *Journal of Medical Virology* published by Wiley Periodicals LLC.

KEYWORDS

ginkgolide B, glutathione peroxidase, long COVID syndrome, nanomedicine, oxidative stress, quercetin

1 | INTRODUCTION

The remarkable success of the COVID-19 vaccines developed by Pfizer-BioNTech (BNT162b2, Comirnaty®) and Moderna (mRNA-1273, Spikevax®) has demonstrated the value and rapid translational potential of nanoparticulate drug delivery systems such as lipid nanoparticles (LNPs).^{1,2} The precision and targeting capabilities of lipid-based nanomedicines offer the potential to enhance therapeutic efficacy and minimize side effects. This opens new opportunities for personalized treatment strategies in managing viral infectious diseases.³ COVID-19 infections also involve long-term neurological complications categorized under the terms “Post COVID syndrome,” “Post-acute sequelae of COVID,” or “neurological long COVID.”^{4–7} Post-COVID conditions are seen among 30%–60% of patients with asymptomatic or mild forms of COVID-19 and currently cause a greater burden of disability in the population than either cancer or heart disease.

Long COVID comprises persistent neurological and neuropsychiatric symptoms (including prolonged memory disorders, headaches, anxiety, depression, loss of taste and smell, muscle and joint pain, fatigue, mental fog, etc.), which emerge months after the onset of the viral infection. In severe COVID-19 cases, the infection can also result in delirium, psychosis, inflammatory syndromes (including encephalitis and acute disseminated encephalomyelitis), and ischemic and hemorrhagic strokes.⁸ The etiology underlying the neurological symptoms associated with COVID is not completely understood yet, but studies showed that the virus can travel to non-respiratory sites including the brain, and can induce oxidative stress and inflammatory response thus, causing neurological symptoms.^{9,10}

Evidence has shown that the damage caused by oxidative stress, such as increased lipid peroxidation and inadequate total antioxidant response, results in lower glutathione peroxidase (GSH-Px) and glutathione reductase (GR) levels and higher serum concentrations of interleukin-10 (IL-10) among patients with SARS-CoV-2 infection. This indicates that impairment of redox homeostasis is responsible for the accumulation of reactive oxygen species (ROS). Accordingly, the antioxidant system plays a crucial role in reducing the increased inflammation that causes COVID-19-induced neurological damage at different levels including radical prevention, radical scavenging, and radical-induced damage repair.¹¹ Therefore, the application of nanomedicine in the management of neurological long COVID offers the advantage of controlled drug delivery systems for single or multiple drug loading and can be suitable in managing post-infectious neurological outcomes through the modulation of redox signaling pathways.

In this work, we propose a nanotherapy approach for restoring the levels of the antioxidant enzyme GSH-Px that is strongly depleted

by the coronavirus infection and of key importance for recovery from neurological long COVID. Our design of a nanotherapy for the inhibition of excessive ROS production and regulation of antioxidant enzyme levels is presented in Figure 1.

Here we chose ginkgolide B (GB), a diterpene derived from the leaves of *Ginkgo biloba*, for nanomedicine development because of its valuable neuroprotective and antioxidant properties. GB is a preferred agent for the treatment of neurological disorders including Parkinson's disease, dementia, and ischemic stroke.^{13,14} Current research on the use of GB nanotherapy in oxidative-stress-related pathologies explores the effect of GB in alleviating hypoxia-induced neuronal damage in rat hippocampus, through inhibiting oxidative stress and apoptosis.

To our knowledge, the therapeutic efficacy of GB-nanomedicines studied alone, or GB co-administered by LNPs with other extracts of *Ginkgo biloba* (such as quercetin), has not been explored in the management of neurological long COVID. The first objective of our work is to develop nanocarrier-mediated drug delivery systems encapsulating *Ginkgo biloba* extract (EGb) of ginkgolide B and quercetin using self-assembled liquid crystalline nanostructures of hydrated monoolein (MO) or 1,2-dimyristoyl-sn-glycero-3-phosphocholine (DMPC).

Our second objective is to evaluate the therapeutic outcome of the novel drug-loaded liquid crystalline LNPs at the molecular level. For this purpose, we established an in vitro disease model mimicking the oxidative stress conditions of neurological long COVID by using potassium persulfate (KPS) as an oxidative-stress inducer in dopaminergic (DAergic) SH-SY5Y cells. Although the exact mechanism of KPS is not fully known (e.g., transient neuronal damage), we hypothesize that it primarily damages dopaminergic neurons through cell death caused by excessive production of ROS and subsequent mitochondrial dysfunction. We then show that the designed nano-antioxidants, when administered to the in vitro cellular model of oxidative stress damage, can inhibit apoptotic and necrotic cell death through a ROS scavenging mechanism. Furthermore, we show that the GB-loaded nanoparticles enhance the levels of the antioxidant enzyme GSH-Px and favor regeneration.

2 | MATERIALS AND METHODS

2.1 | Materials

Ginkgolide B (GB), quercetin (Quer), diacetyldichlorofluorescein (DCFH-DA), 2,2-Diphenyl-1-picrylhydrazyl (DPPH), Pluronic F127, monoolein (MO, C18:1c9, powder, ≥99%), retinoic acid (RA), butylated hydroxy-toluene (BHT) were purchased from Sigma-Aldrich. The phospholipid,

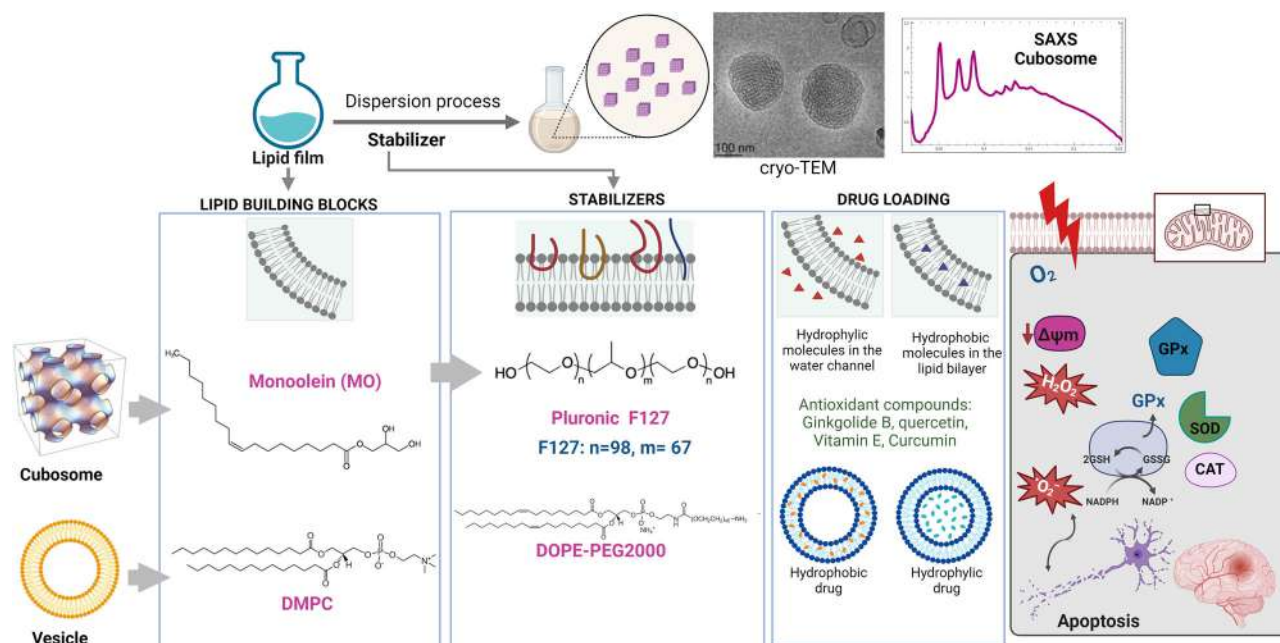


FIGURE 1 Schematic representation of the engineering process of lipid nanoparticles (LNPs) of cubosome and vesicle types by a self-assembly method in view of nanomedicine applications aiming at ROS clearance and regulation of antioxidant enzymes glutathione peroxidase (GPx), catalase (CAT), or superoxide dismutase (SOD). Lipid building blocks include a nonlamellar lipid monoolein MO (to obtain liquid crystalline structures such as cubosomes) or a lamellar phospholipid DMPC (to obtain a vesicle-type of nanocarriers). The nanostructures are stabilized by Pluronic F127 or DOPE-PEG₂₀₀₀ amphiphiles. Drug loading is achieved within the lipid membrane compartments or localized within the water core compartments depending on the Log P (hydrophobicity/hydrophilicity) characteristics of the encapsulated bioactive compounds. The cryo-TEM image (reproduced with permission from Ref. [12]) and the SAXS pattern are characteristic of a cubosome-type of LNPs (top right panel). The bottom right panel summarizes the key processes during oxidative stress damage of living cells.

1,2-dimyristoyl-sn-glycero-3-phosphocholine (14:0 DMPC) and the surfactant 1,2-dioleoyl-sn-glycero-3-phosphoethanolamine-N-[methoxy (polyethylene glycol)-2000] (ammonium salt) (18:1 PEG₂₀₀₀ PE) were purchased from Avanti Polar Lipids. Water of MilliQ quality (Millipore Corp., Molsheim, France) was used for preparation of a phosphate buffer solution ($\text{NaH}_2\text{PO}_4/\text{Na}_2\text{HPO}_4$, 1×10^{-2} M, pH 7, p.a. grade, Merck).

2.2 | Preparation of lipid nanoparticles

Lipid nanoparticles were prepared by self-assembly via hydration of a lyophilized mixed thin lipid film followed by physical agitation in excess aqueous phase. The lipids, including MO, DMPC, and DOPE-PEG₂₀₀₀ along with the surfactant Pluronic, as well as the active compounds GB and quercetin (Quer), were weighed at desired proportions and dissolved in chloroform under a fume hood. The samples were prepared at room temperature at four different lipid-to-drug ratios (MO-GB, MO-GB-Quer, DMPC-PEG-GB, and DMPC-PEG-GB-Quer) as indicated in Table S1. The chloroform solvent was then evaporated under a stream of nitrogen gas for 1 h at room temperature to form a thin lipid film. To remove any excess organic solvent, the samples were lyophilized overnight. The thin film samples were hydrated at room temperature in a solution of 1×10^{-2} M phosphate buffer (ph.b) stabilized with butylated hydroxytoluene (BHT) prepared with Milli-Q water. The mixture was

fragmented and homogenized for 15 min using an ultrasonic ice bath and a frequency of 42 kHz. This process facilitates the self-assembly of cubosome and vesicle types of liquid crystalline nanoparticles at room temperature (22°C).

2.3 | Nanoparticles size determination

The size distributions of the LNPs were measured using a Nano-ZS90 device from Malvern Instruments. The samples were dispersed in excess aqueous phase and subjected to laser beam illumination, while the intensity of the scattered light was measured at a 90° angle by a fast photon detector. The data collection process was conducted in triplicate at a temperature of 25°C. The refractive index and viscosity of the Milli-Q water were 1.330 and 0.8872, respectively.

2.4 | Synchrotron Small-Angle X-ray Scattering (SAXS)

SAXS measurements were performed at the SWING beamline of synchrotron SOLEIL (Saint Aubin, France). The wavevector is defined as $q = 4\pi \sin(\theta)/\lambda$, where 2θ is the angle between the incident and the scattered X-rays and λ is the wavelength. The

synchrotron radiation wavelength was $\lambda = 1.033 \text{ \AA}$, and the exposure duration was set at 500 ms. Calibration of the q -range was conducted using a standard sample of silver behenate with a repeat spacing of $d = 58.38 \text{ \AA}$.

The dimensions of the X-ray beam spot applied to the samples were $375 \times 25 \mu\text{m}^2$. Patterns were acquired using a two-dimensional Eiger X 4 M detector (Dectris, Baden-Daettwil Switzerland) at 12 keV, enabling measurements within the q -range of $0.0179\text{--}2.18 \text{ \AA}^{-1}$.¹⁵ The samples were filled in X-ray capillaries with a diameter of 1.5 mm. The samples were placed in a designed holder with (X, Y, Z) positioning. An average of five spectra was obtained per sample. The experiments were performed at 22°C. The SAXS pattern of a background sample, composed of ph.b. with pH 7.0, was subtracted from all the samples. The data analysis was performed using ATSAS 3.2.1 software suite with the PRIMUS feature.

The lattice parameters of the liquid crystalline lipid phases were deduced by analyzing the Bragg peaks identified in the X-ray diffraction patterns. For cubic phases, the lattice parameter a_0 , is determined by the formula $a = d (h^2 + k^2 + l^2)^{1/2}$, where the d -spacing (d) is defined by Bragg's law, $d = 2\pi/q$, representing the repeat distance between the scattering planes (i.e., $1/d^2 = (h^2 + k^2 + l^2)/a^2$).¹⁵ The assigned reflections were fitted based on the Miller indices (hkl).

For structures with a lamellar spacing, the relationship is expressed as $a/d = 1, 2, 3, \dots$

For cubic structures of the primitive (P) type ($Im3m$ space group), the relationship follows the sequence $(a/d)^2 = 2, 4, 6, 8, 10, 12, 14, 16, 18, 20, 22, \dots$

2.5 | DPPH free radical scavenging activity assay

The free radical scavenging capacity of the LNPs were measured by the 2,2-diphenyl-1-picrylhydrazyl (DPPH) assay. We tested the nanoparticles at a concentration of $1 \times 10^3 \mu\text{M}$ at different time intervals (15–150 min). In addition, the same concentration was tested for Trolox (Cat. #. 648471, Millipore Corp, USA), serving as a reference standard substance. Before the assay, a stock solution of DPPH (80 μM) was prepared in ethanol and stored in darkness at room temperature. Briefly, 50 μl of LNP samples were mixed with 150 μl DPPH solution in a 96 well plate. Samples were initially incubated in the dark for 5 min and the reaction was monitored every 15 min for a total incubation time of 150 min. The absorbance was measured at a wavelength of 517 nm using a microplate reader.¹⁶ The antioxidant capacity was determined as a percentage of DPPH radical scavenging capacity using the following formula:

$$\text{Inhibition (\%)} = \frac{A_0 - A_1}{A_0} \times 100$$

where A_0 and A_1 are the absorbances of the control and test samples, respectively.

2.6 | Reducing antioxidant power of LNPs (CUPRAC assay)

The CUPRAC method evaluates the capacity of antioxidants to reduce Cu^{2+} to Cu^+ . Conveniently, commercially available kits allow for microscale spectrophotometric measurements using 96-well plates. This assay specifically quantifies the total antioxidant capacity (TAC) of a sample. It relies on the formation of a colored complex between the resulting Cu^+ and a dye reagent. The intensity of the color at 570 nm is directly proportional to the TAC of the sample. The absorbance measurements for the standard (Trolox) and sample were performed in duplicate using an Antioxidant Assay Kit (Cat. #. MAK334, Sigma-Aldrich, France). The measurement was performed by adding 20 μl of LNPs at a total lipid concentration of $1 \times 10^3 \mu\text{M}$ to 100 μl Reaction Mix and incubated for 10 min at room temperature. The absorbance values were compared to a calibration curve generated for the reference substance, Trolox. The calibration curve demonstrated linearity within the range of 300–1000 μM . The TAC values of the examined samples were calculated according to the following equation:

$$\text{TAC } (\mu\text{M}) = 1 + \frac{(\text{A570})_{\text{sample}} - (\text{A570})_{\text{blank}}}{\text{SLOPE } (\mu\text{M}^{-1})} \times n$$

where $(\text{A570})_{\text{sample}}$ represents the absorbance of the sample, $(\text{A570})_{\text{blank}}$ is the absorbance of the medium blank, n stands for sample dilution factor, and Slope is related to a linear calibration curve prepared for the reference substance.

2.7 | Oxygen Radical Absorbance Capacity assay (ORAC)

The oxidative properties of KPS were compared to 2,2'-azobis(2-amidinopropane) dihydrochloride (AAPH), a water-soluble azo initiator often employed in the study of lipid peroxidation and characterization of antioxidant compounds. The ORAC assay was performed in a 96-well plate using an Antioxidant Assay Kit (Cat. #. STA-345, Cell Biolabs, INC). In brief, 180 μl of fluorescein (FL) solution and 25 μl of various concentrations of the antioxidant Trolox (2.5, 5, 10, 20, and 40 μM) were added to each experimental well and incubated for 30 min at 37°C. The reaction was initiated by introducing either AAPH or KPS at a concentration of 294 mM and gently shaking the plate to homogenize the sample. Fluorescence intensity was recorded every minute for a duration of 60 min ($\lambda_{\text{excitation}} = 488 \text{ nm}$; $\lambda_{\text{emission}} = 520 \text{ nm}$).¹⁷ Oxidation of FL in the absence of a radical source was also evaluated by replacing AAPH/KPS solution with assay diluent, which served as a blank. Solutions containing antioxidants were analyzed in duplicate. All fluorescence measurements were carried out at 37°C using FLUOstar OPTIMA microplate reader.

The area under the curve (AUC) was calculated from the following equation:

$$\text{AUC} = 1 + \text{RFU}_1/\text{RFU}_0 + \text{RFU}_2/\text{RFU}_0 + \text{RFU}_3/\text{RFU}_0 + \dots + \text{RFU}_{59}/\text{RFU}_0 + \text{RFU}_{60}/\text{RFU}_0,$$

where Net AUC = AUC (Antioxidant) – AUC (blank), RFU_0 = relative fluorescence value of a time point zero, and RFU_x = relative fluorescence value of time points (minutes).

2.8 | Cell culture

The differentiated human neuroblastoma cells (SH-SY5Y) were used as an in vitro model. Cell culture was regularly maintained in a 5% CO₂ incubator at 37°C in Dulbecco's modified Eagle's Medium (DMEM), with high glucose and supplemented with 10% Fetal bovine serum (FBS) and 1% streptomycin-penicillin (Pen/Strep). Phosphate buffered saline, deficient of calcium and magnesium ions (PBS), FBS, Pen/Strep, trypsin, dimethyl sulfoxide (DMSO), and 3-(4,5-Dimethylthiazol-2-yl)-2,5-diphenyl tetrazolium bromide (MTT) were supplied from Sigma-Aldrich. Cellular differentiation was done by incubation with 10 μ M retinoic acid (RA) for 5 days.

2.9 | Evaluation of the in vitro neurotoxic activity of the oxidative agent potassium persulfate (KPS)

The ability of the KPS to induce oxidative stress and nerve cell death was determined by the tetrazolium dye assay (3-(4,5-dimethylthiazol-2-yl)-2,5-diphenyl tetrazolium bromide (MTT), Annexin-V-FLUOS staining kit (Cat. #. 11858777001, ROCHE), Human tyrosine hydroxylase (TH) ELISA kit (Cat. #. KTE60519, Abbkine), and mitochondrial membrane potential JC-10 assay (Cat. #. MAK 160-1KT, Sigma-Aldrich) according to the established procedures.^{18,19} The solution of MTT was prepared in PBS at a concentration of 5 mg/ml and was filtered before use. The mitochondrial succinate dehydrogenase enzyme present in living cells can reduce the tetrazolium dye to a purple formazan crystal, the quantity of which is proportional to the metabolic activity of the living cells. In the MTT assay, SH-SY5Y cells were cultured in 96-well plates at a density of 2.0×10^4 cells/well. Cells were differentiated with 10 μ M retinoic acid (RA) over 5 days following incubation with KPS at a concentration of 50 and 100 mM at different time intervals. Untreated SH-SY5Y cells maintained in FBS-free medium (10 μ M RA) were used as negative controls. After 1 h of incubation of the cells with MTT, the medium was removed, and the insoluble formazan salt formed was dissolved in a solubilizing agent (100% DMSO). The colored product was quantitatively measured at 570 nm by a microplate reader. The quantification was done using measurements of a minimum of 12 wells.

For bioassays of apoptosis, necrosis, mitochondria membrane potential (MMP) changes, and tyrosine hydroxylase expression, cells were seeded at a density of 3.0×10^5 cells in 6-well plates or 5.0×10^6 depending on the type of biological analysis to be carried out. The SH-SY5Y cells were cultured in DMEM with high glucose supplement, 10% FBS, and 0.5% streptomycin/penicillin. After 24 h, the cell culture medium was replaced by 10 μ M RA solution for 5 days of incubation. The cells were treated with 50 mM KPS for 30 min after which they were washed with PBS and collected by trypsinization. The pelleted

cells were resuspended in 100 μ l Annexin-V-FLUOUS labeling solution or JC-10 loading solution, containing JC-10 assay buffer, and incubated for 15 min at room temperature to evaluate apoptosis/necrosis or MMP changes, respectively. The stained cells were analyzed on the BD C6 Accuri flow cytometer using the FL-1 channel (Ex. 488 nm/Em 530 nm) for green fluorescence and the FL-2 channel (Ex. 488 nm/Em 578 nm) for red fluorescence signal. The JC-10 dye probe is aggregated in the mitochondria of normal cells. The corresponding J-aggregates are characterized by red fluorescence. The monomeric form of the JC-10 dye is characterized by green fluorescence. The monomeric dye is released from the mitochondria when the MMP is decreased. In the MMP assay, the experimental data are expressed as fluorescence intensity ratios [red (FL2)/green (FL1)] representing the state of the JC-10 dye in the cells.

The tyrosine hydroxylase (TH) expression was evaluated in SH-SY5Y cells seeded into 75 cm² flasks at a density of 5×10^6 cells. Cells were differentiated with 10 μ M RA for 5 days and incubated with 50 mM KPS for 30 min. After KPS treatment, cells were lysed with lysis reagent, CellLytic™ M (Cat. #. C2978, Sigma-Aldrich) and collected. Samples were centrifuged for 15 min at 1200 rpm and the supernatant was collected for assaying according to the manufacturer's protocol (TH protein ELISA kit).

2.10 | Intracellular ROS detection by flow cytometry

The analysis of intracellular ROS was carried out utilizing flow cytometry. To accomplish this, a nonfluorescent cell-permeant compound, DCFH-DA was used. DCFH-DA is hydrolyzed by esterase, resulting in the formation of DCFH. Oxidation of DCFH by ROS converts the molecule to DCF, which emits green fluorescence at an excitation wavelength of 488 nm and an emission wavelength of 533 nm.²⁰⁻²² The intensity of fluorescence observed is directly proportional to the production of ROS. The detection of intracellular ROS in cells subjected to KPS-induced oxidative stress or treated by LNP nanoformulations was achieved in the FL-1 channel. The measurements were carried out after 30 min of incubation of the SH-SY5Y cells with 10 μ M of DCFH-DA in FBS-free medium at 37°C. The cellular treatment with KPS and LNPs was performed in two modes: (i) pretreatment with 1 μ M LNPs for 24 h followed by induction of ROS using 5 min incubation with KPS at a concentration of 50 mM, and (ii) treatment with 1 μ M LNPs for 24 h after exposure to 50 mM KPS for 30 min.

2.11 | Determination of glutathione peroxidase (GSH-Px) enzymatic activity in SH-SY5Y cell lysates

The glutathione peroxidase (GSH-Px) activity was measured in differentiated SH-SY5Y cells, which were seeded into 75 cm² flasks at a density of 5×10^6 cells. The total concentrations of GSH-Px in cell lysates were determined by using GSH-Px assay kit from Cayman Chemical Co. (Cat. #. 703102, Ann Arbor, MI). GSH-Px activity is

measured indirectly through a coupled reaction involving glutathione reductase (GR). The oxidized glutathione (GSSG) generated by the reduction of H_2O_2 by GSH-Px, is recycled back to its reduced form by GR and NADPH (see Figure 6A). During this process, NADPH is oxidized to NADP^+ , resulting in a decrease in absorbance at 340 nm which is directly proportional to the GSH-Px activity detected in the sample.^{12,23–25} Before assaying, SH-SY5Y cells were seeded at a density of 5.0×10^6 cells in 75 cm^2 culture flasks containing 15 ml of DMEM medium. Following 5 days of treatment of cells with 10 μM RA solution, the cells were (i) incubated with 1 μM LNPs for 24 h, and (ii) cells were treated with 1 μM LNPs after oxidative stress damage with 50 mM KPS for 30 min. The cells were lysed with CellLytic M mammalian cell lysis buffer (Cat. #. C2978, Sigma-Aldrich) and collected by centrifugation at 1500 g for 15 min at 4°C. The assay was performed with the cell lysates according to the manufacturer's instructions.

2.12 | Apoptosis and necrosis analysis after treatment with GB-loaded LNPs

We assessed the impact of GB-loaded LNPs on apoptosis/necrotic cell death via Annexin-V-FLUOUS staining. SH-SY5Y cells were seeded into 6-well plates at a density of 3.0×10^5 cells. Cells were differentiated with 10 μM RA for 5 days and incubated with 50 mM KPS for 30 min. Subsequently, they were treated with 1 μM GB-loaded LNPs for 24 h, washed with PBS, and collected by trypsinization. The pelleted cells were resuspended in 100 μl Annexin-V-FLUOS labeling solution and incubated at room temperature for 15 min. The stained cells were analyzed on the BD C6 Accuri flow cytometer.

2.13 | Total protein concentration

The total protein concentration within cell lysates was assessed using the Bradford Protein Assay, implemented in 96-well plates. A PBS-based stock solution of bovine serum albumin (BSA) at a concentration of 2 mg/ml was prepared to establish a calibration range with seven BSA concentrations, serving as a reference. In each well, 20 μl of either BSA standard solutions or cell lysate samples were mixed with 180 μl of Bradford reagent (Sigma, B6916-500ML). Subsequently, the absorbance of each well was measured using a microplate reader at a wavelength of 595 nm, with the optical density of a blank well subtracted. To normalize the protein amounts in GSH-Px and TH analyzed samples, the protein concentration values calculated for GSH-Px and TH samples were divided by the total protein concentration measured in each respective sample.²⁶

2.14 | Statistical analysis

Statistical analysis was conducted using GraphPad prism version 8.0.1 analysis software. The data were presented as the mean \pm SD. Statistical significance was evaluated by Independent Student's *t* test

for comparison of two groups, one-way ANOVA or two-way ANOVA for multiple groups. *p* values of <0.05 were considered statistically significant. Cytometry dot plot were obtained using Flowjo software, version 10.8.1.

3 | RESULTS

3.1 | Lipid nanoparticles loaded with ginkgolide B and quercetin

We explored both lamellar and nonlamellar lipid compositions to obtain nanoparticulate systems (LNPs) suitable for the neurotherapeutic management of oxidative stress associated with long COVID. Nonlamellar lipid phases serve as valuable drug-delivery nanomaterials due to their ability to self-assemble into liquid crystalline mesophases in an aqueous environment, creating structures with both hydrophilic and hydrophobic compartments.^{27–30} Monoolein (MO), an uncharged single-chain amphiphile with an ester linkage, was used as a nontoxic monoacylglycerol that forms nonlamellar lipid cubic phases.^{31–34} For comparison, DMPC was employed as a lamellar type of phospholipid forming vesicle drug delivery nanocarriers (detailed in Table S1). The nanocarriers loaded with GB or co-loaded with GB and quercetin were stabilized by the surfactant agents Pluronic F127 or DOPE-PEG₂₀₀₀ (Table S1). The lipid/antioxidant systems were fully hydrated in an excess aqueous phase of 1×10^{-2} M phosphate buffer (ph.b) of pH 7.0.

Synchrotron SAXS measurements were conducted to investigate the nanostructural organization, lattice parameters, and phase types of the liquid crystalline particles formed in the lipid nanodispersions. Figure 2A–C shows the SAXS patterns of nonlamellar and lamellar types of LNPs obtained at a temperature of 22°C. The blank (DMPC-PEG) and the dual-drug loaded vesicular systems did not display Bragg reflections emerging from long-range order in the lipid bilayer organization. These results indicated that the DMPC lipid membranes were dispersed into unilamellar vesicles stabilized by PEGylation. The obtained SAXS profiles (lower plots in Figure 2A–C) correspond to the form factor of the generated vesicles with size populations for blank and drug-loaded (GB or GB-quercetin) polydisperse LNP systems presented in Figure 2D.

The size distributions of the investigated nano-antioxidant dispersions were determined using quasi-elastic light scattering (QELS) measurements. The results are presented in Figure 2D and Table 1 referring to the mean particle hydrodynamic diameters (D_h) derived from intensity distributions.

3.2 | In vitro antioxidant capacity of LNP-based nano-antioxidants determined by DPPH and CUPRAC assays

The antioxidant activity of GB-loaded and GB-Quer-loaded LNPs was determined using two independent methods DPPH and CUPRAC

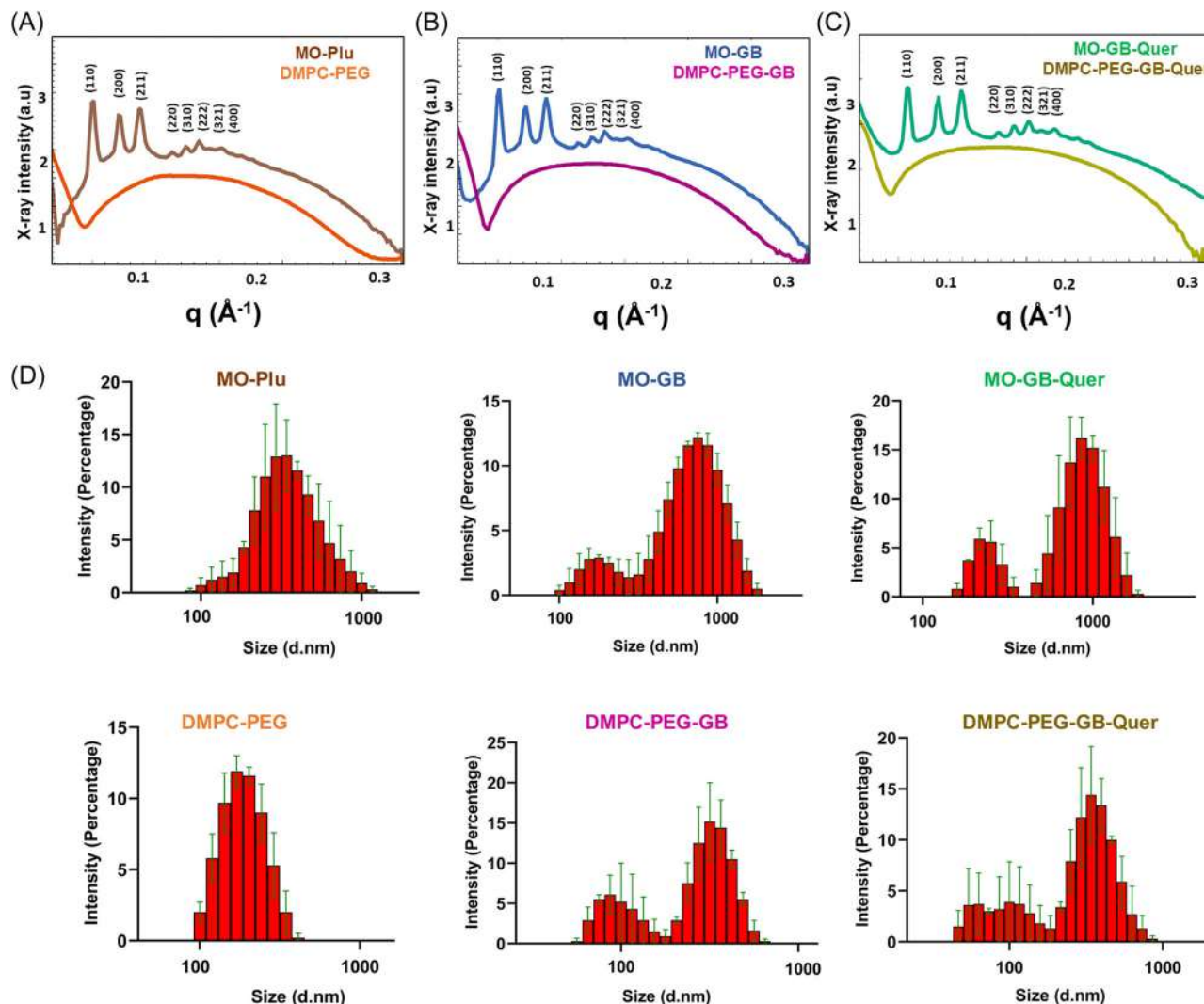


FIGURE 2 Structural and nanosize characterization of cubosomal and vesicular ginkgolide B (GB)-loaded liquid crystalline lipid nanoparticles (GB-LNPs) as well as co-loaded GB-Quer-LNPs. (A–C) BioSAXS patterns of blank MO-Plu and DMPC-PEG (A), GB-loaded MO (MO-GB) and DMPC-PEG-GB (B), and dual-loaded MO-GB-Quer and DMPC-PEG-GB-Quer (C) nanoassemblies. (D) Size distributions of liquid crystalline LNPs determined by quasi-elastic light scattering (QELS). Data are presented as % mean intensity \pm SD.

(Figure 3). The reaction of GB-loaded LNPs with DPPH• reagent was monitored at 340 nm in 15-min intervals for 150 min. Free radical scavenging activity, calculated for each concentration at each point, was expressed as percentage (%) inhibition and represented as a function of time (Figure 3A). The blank vesicles (DMPC-PEG) and cubosomes (MO-Plu) showed the least activity. The dual-loaded MO-GB-Quer and DMPC-PEG-GB-Quer LNPs exhibited the highest activity at 150 min, corresponding to free radical inhibition of 67% and 81%, respectively (Figure 3B). The scavenging activity of MO-GB and DMPC-PEG-GB was below 50%.

The reducing power of the LNPs after encapsulating GB (3% w/w) or GB and quercetin (3:2% w/w) increased with increasing antioxidant concentrations and showed statistically significant greater values as compared to the blank nanocarriers.

The reduction of Cu(II) to Cu(I) ions is often employed to measure electron donation, which comprises an important antioxidant

mechanism. We determined the ability of antioxidant-loaded LNPs to reduce Cu(II) to Cu(I) by using copper(II) neocuproine reagent as a chromogenic oxidant at 570 nm.³⁵ Figure 3C depicts the total antioxidant capacity (TAC) of the studied LNP formulations.

3.3 | Cellular model of potassium persulfate (KPS)-induced oxidative stress damage in differentiated SH-SY5Y cells

The use of KPS to investigate the mechanism of oxidative stress damage relevant to neurological long COVID syndrome is explored here for the first time. The precise mechanism by which KPS generates ROS and induces toxicity is not fully known. Various in vitro and in vivo models have been previously studied to comprehend the molecular pathways of neuronal death and to develop strategies for neuroprotection/

TABLE 1 Cubic unit cell lattice parameters, $a_{(Q)}$, determined from SAXS experiments, mean hydrodynamic diameters (D_h), and polydispersity indices of GB-loaded or GB-Quer loaded MO- and DMPC-based lipid nanoparticles (LNPs) obtained by spontaneous self-assembly and dispersion of hydrated lipid mixtures stabilized by Pluronic F127 or DOPE-PEG₂₀₀₀.

GB-loaded and GB-Quer loaded LNPs	Cubic Im3m lattice parameter $a_{(Q)}$ (nm)	Hydrodynamic size (nm)	PDI
MO-Plu	17.45	342 ± 5	0.289
MO-GB	17.39	190/825 ± 1/3	0.350
MO-GB-Quer	16.84	220/825 ± 2/3	0.451
DMPC-PEG	—	164 ± 1	0.460
DMPC-PEG-GB	—	91/342 ± 3/6	0.451
DMPC-PEG-GB-Quer	—	106/342 ± 5/7	0.464

neuroregeneration. Many of these models involve the use of experimental neurotoxins such as 6-hydroxydopamine (6-OHDA), 1-methyl-4-phenyl-1,2,3,6-tetrahydropyridine (MPTP), hydrogen peroxide (H_2O_2), and tunicamycin.^{27,35} These neurotoxins can induce toxicity and replicate the neuropathological and biochemical features of neurodegenerative diseases like Alzheimer's and Parkinson's diseases at the cellular level.

Here we developed an in vitro oxidative stress model to mimic a similar effect during post-COVID-19 neuronal damage. For this purpose, the effect of KPS on oxidative stress damage was evaluated in the SH-SY5Y cellular model (characteristic of DAergic neurons) via MTT and apoptosis/necrosis assays, GSH-Px enzymatic activity, mitochondria membrane potential changes ($\Delta\Psi_m$), and the expression of TH protein (Figure 4). In the assessment of ROS and cell metabolic activity, the human neuroblastoma cells were exposed to concentrations of 50 mM and 100 mM KPS over a 2 h period. The treatment with the chosen concentrations of KPS resulted in an increased generation of ROS and induction of neurotoxicity in a dose- and time-dependent manner, from 5 to 120 min (Figure 4A, B). This suggested that dopaminergic neuronal cells exhibit a high susceptibility to KPS and oxidative stress-induced cell death that is attributed to excessive free radical generation.

Moreover, the performed microscopic investigations revealed that cellular exposure to both concentrations of KPS led to a morphological transition from elongated neuritic outgrowth projections to a more rounded shape (Figure 4C). This morphological change suggested the initiation of an apoptotic/cell death process. Oxidative stress is characterized by the elevation of intracellular ROS [superoxide anion ($O_2^{\bullet-}$), H_2O_2 , and hydroxyl radical ($^{\bullet}OH$)] and reactive nitrogen species (RNS) (nitric oxide (NO) and peroxynitrite ($ONOO^-$)) that cause damage to lipids, proteins, and DNA.^{36–44} In creating our disease model, we considered that neuroinflammation and oxidative stress play major roles in modulating the signaling cascade that activates astrocytes

and microglia, resulting in the onset of neurodegenerative disorders and other neurological diseases.⁴⁵

Based on the performed ROS experiments (Figure 4B) and MTT assays (Figure 4A), we adopted the condition of 50 mM KPS (for 30 min) to mimic acute oxidative stress neuronal damages for all subsequent studies with the neuro-COVID in vitro model. Oxidative stress and mitochondrial dysfunction caused by KPS is expected to induce redox-sensitive targets including apoptotic/necrotic events, loss in neurite function, decrease in TH protein levels, and depletion of endogenous antioxidant markers such as GSH-Px. We evaluated the effect of KPS on all these biomarkers to determine the extent of oxidative stress in the studied cells.

The results presented in Figure 4D–G show that the exposure of SH-SY5Y cells to KPS resulted in a significant reduction in GSH-Px activity (Figure 4F), decreased TH protein expression (Figure 4E), and an increase in cell death/apoptosis (Figure 4G) accompanied by an altered mitochondria membrane potential as compared to the control group RA/FBS(–) (Figure 4D). Figure S1 shows additional data about the oxidative properties of KPS.

3.4 | Ginkgolide B-loaded cubosomes and vesicles reduce KPS-induced apoptotic and necrotic cell death

Cellular viability data after incubation with MO-GB and DMPC-PEG-GB LNPs are presented in Figure S2. A lipid concentration of 1 μ M was nontoxic for the differentiated SH-SY5Y cells.

The protective effect of GB-loaded LNPs against KPS-induced cell death was analyzed by flow cytometry using the Annexin V-fluorescein isothiocyanate (FITC) and propidium iodide (PI) staining, a method employed to distinguish viable and nonviable cell populations. As shown in Figure 5A, the incubation of differentiated SH-SY5Y cells with KPS for 30 min (i.e., oxidative challenge) augmented the percentage of cells in an apoptosis state (by 32.6%, Annexin V + /PI–) as well as in a necrosis state (by 8.45%, Annexin V–/PI +). The treatment with 1 μ M cubosome nanocarriers (MO-GB or MO-GB-Quer LNPs) and vesicles (DMPC-PEG-GB or DMPC-PEG-GB-Quer LNPs) for 24 h reduced the number of cells undergoing apoptosis by 19.0%, 12.8%, 14.8%, and 23.6%, respectively, and necrosis by 5.9%, 2.0%, 2.4%, and 3.6%, respectively (Figure 5B–D). Thus, our results demonstrated that KPS, as a neurotoxin stressor, significantly induces programmed cell death, as evidenced by Annexin V/PI staining data. This effect was reversed by the treatment of GB-loaded LNPs.

3.5 | Effects of ginkgolide B-loaded cubosomes and vesicles on the GSH-Px activity in KPS-induced model of oxidative stress damage

We evaluated the effect of GB-loaded cubosomes and vesicles on the levels of the antioxidant enzyme GSH-Px in SH-SY5Y cells using two distinct procedures (Figure 6). First, SH-SY5Y cells were incubated with different types of LNPs in the absence of a neurotoxic agent. This initial

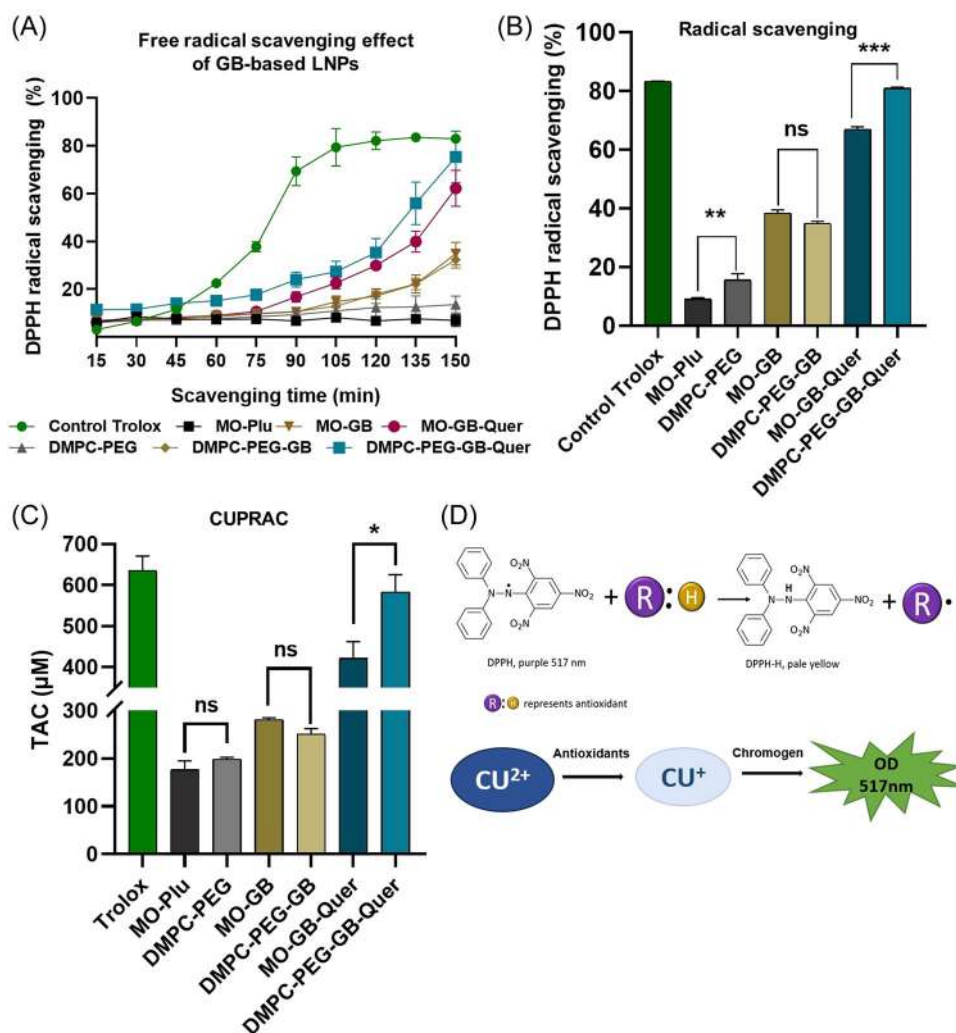


FIGURE 3 In vitro antioxidant capacity of cubosome and vesicular types of LNPs. (A) Temporal evolution, and (B) quantitative histogram of antioxidant activity of GB-loaded and GB-Quer-loaded LNPs expressed as mean (%) of DPPH radical inhibition ($n = 2$). All p -values are indicated with $p < 0.05$ considered as statistically significant. $ns = 0.092$, $**p = 0.004$ for MO-Plu versus DMPC-PEG, $***p < 0.0001$ for MO-GB-Quer versus DMPC-PEG-GB-Quer. (C) Total antioxidant activity of GB-loaded and GB-Quer-loaded LNPs expressed as mean Trolox equivalent. inhibition ($n = 2$). $ns = 0.099$ and 0.980 for MO-Plu versus DMPC-PEG and MO-GB versus DMPC-PEG-GB respectively, $*p = 0.038$ for MO-GB-Quer versus DMPC-PEG-GB-Quer. (D) Schematic presentation of DPPH and TAC assay principles. n represents the number of replicates per group, with error bars indicating the standard deviation. Statistical differences were calculated using Tukey's multiple comparison test for one-way ANOVA.

experiment aimed to evaluate the direct influence of lipid nanoparticles on GSH-Px activity. The results depicted in Figure 6B demonstrate a significant increase in GSH-Px activity compared to the GSH-Px control. Notably, GB-loaded cubosomes (MO-GB) exhibited a statistically significant enhancement in GSH-Px activity compared to DMPC-PEG-GB vesicles, with p -values of 0.0007 and 0.0074, respectively. Furthermore, the co-encapsulation of GB/Quer within the MO cubosome nanocarrier resulted in a marginal improvement in GSH-Px activity compared to dual-loaded DMPC-PEG-GB-Quer vesicles ($p = 0.0006$ and $p = 0.0007$). This highlighted the potential antioxidative and neuroprotective properties of the liquid crystalline nanoparticles used for drug delivery.

In a subsequent experiment, SH-SY5Y cells were exposed to 50 mM KPS followed by treatment with 1 μM GB-loaded cubosomes and vesicles for 24 h. Similarly, the results showed a remarkable increase in the levels of the GSH-Px enzyme, particularly for MO-GB,

$p = 0.0003$ (Figure 6C, D) compared to the KPS-induced SH-SY5Y cells. These findings suggested that LNP treatment can ameliorate the enzymatic antioxidant activity of GSH-Px under normal and oxidative stress conditions by eliminating additional hydroperoxides and free radicals as depicted in the scheme of Figure 6A.

We further investigated the neuroprotective potential of antioxidant-loaded LNPs in attenuating ROS levels in a KPS-induced oxidative stress model using flow cytometry (Figure 6E, F). We employed two distinct procedures for KPS exposure. First, cells were pretreated with 1 μM LNPs in serum-free DMEM before incubation with DCFH-DA probe (10 μM) for 30 min. Following flow cytometry analysis, cells were exposed to 50 mM KPS for 5 min. The obtained data revealed an elevation in the fluorescence intensity of DCF upon direct exposure of the cells to 50 mM KPS, in comparison to the unexposed control cells (Figure 6E). Therefore, pretreatment

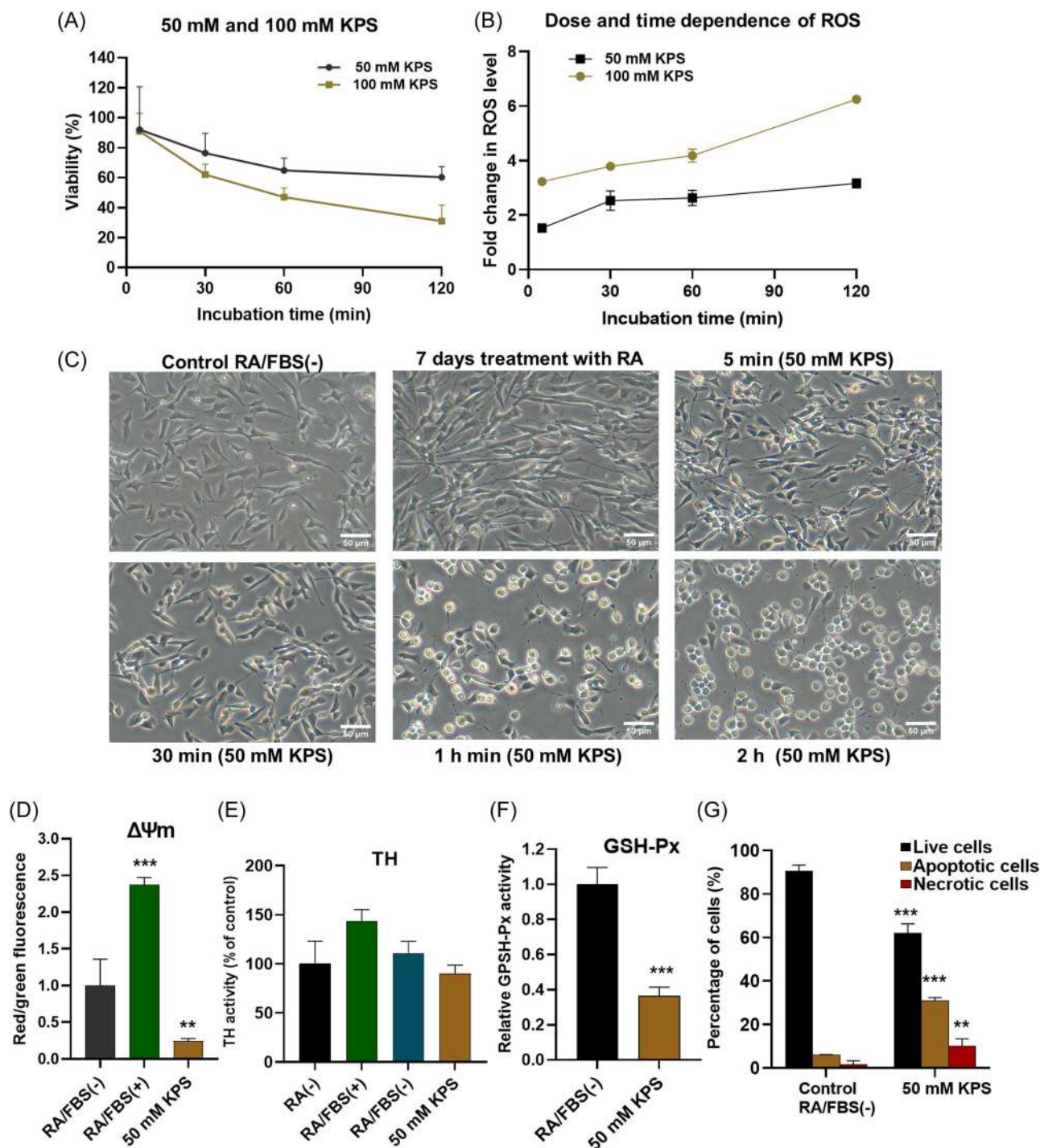


FIGURE 4 In vitro oxidative-stress model induced by KPS in differentiated SH-SY5Y cells. (A) Time course for the effect of KPS on mitochondrial activity via MTT assay. SH-SY5Y cells were pretreated with KPS at concentrations of 50 mM and 100 mM. Results are represented as % mean \pm SD values ($n = 12$). (B) Flow cytometry analysis of ROS generation expressed as a fold change in ROS levels ($n = 3$). (C) Morphology of SH-SY5Y cells observed before and after 7 days of treatment with 10 μ M RA following incubation with KPS at different time points (5 min, 30 min, 1 h, and 2 h). The scale bars are 50 μ m. (D) Mitochondrial membrane potential ($\Delta\Psi_m$) changes of RA/FBS(-)-SH-SY5Y and RA/FBS(+)-SH-SY5Y cells after 30 min of incubation with 50 mM KPS. Results are presented as the ratio of the fluorescence intensities of JC-10 dye aggregates (red fluorescence) to JC-10 dye monomers (green fluorescence) and yielding mean values \pm SD ($n = 3$, $**p = 0.009$, $***p = 0.0004$). Statistical differences were calculated using Dunnett's multiple comparison test for two-way ANOVA. (E) Quantification of the levels of TH protein in the cells. Data are presented as % mean \pm SD ($n = 3$). (F) Effect of KPS on GSH-Px enzymatic activity. Data are reported as mean \pm SD values relative to the control ($n = 3$, $***p = 0.0005$). Statistical differences were calculated using the student's t -test. (G) Flow cytometry assessment of apoptosis and necrosis of SH-SY5Y cells after 30 min treatment with KPS. Cells were stained with Annexin V conjugate and propidium iodide. Data are reported as mean \pm SD values of % cells in live, apoptotic, and necrotic states ($n = 3$, $**p = 0.006$, $***p < 0.0001$). n represents the number of replicates per group, with error bars indicating the standard deviation. Statistical differences were calculated using Bonferroni's multiple comparison test for two-way ANOVA.

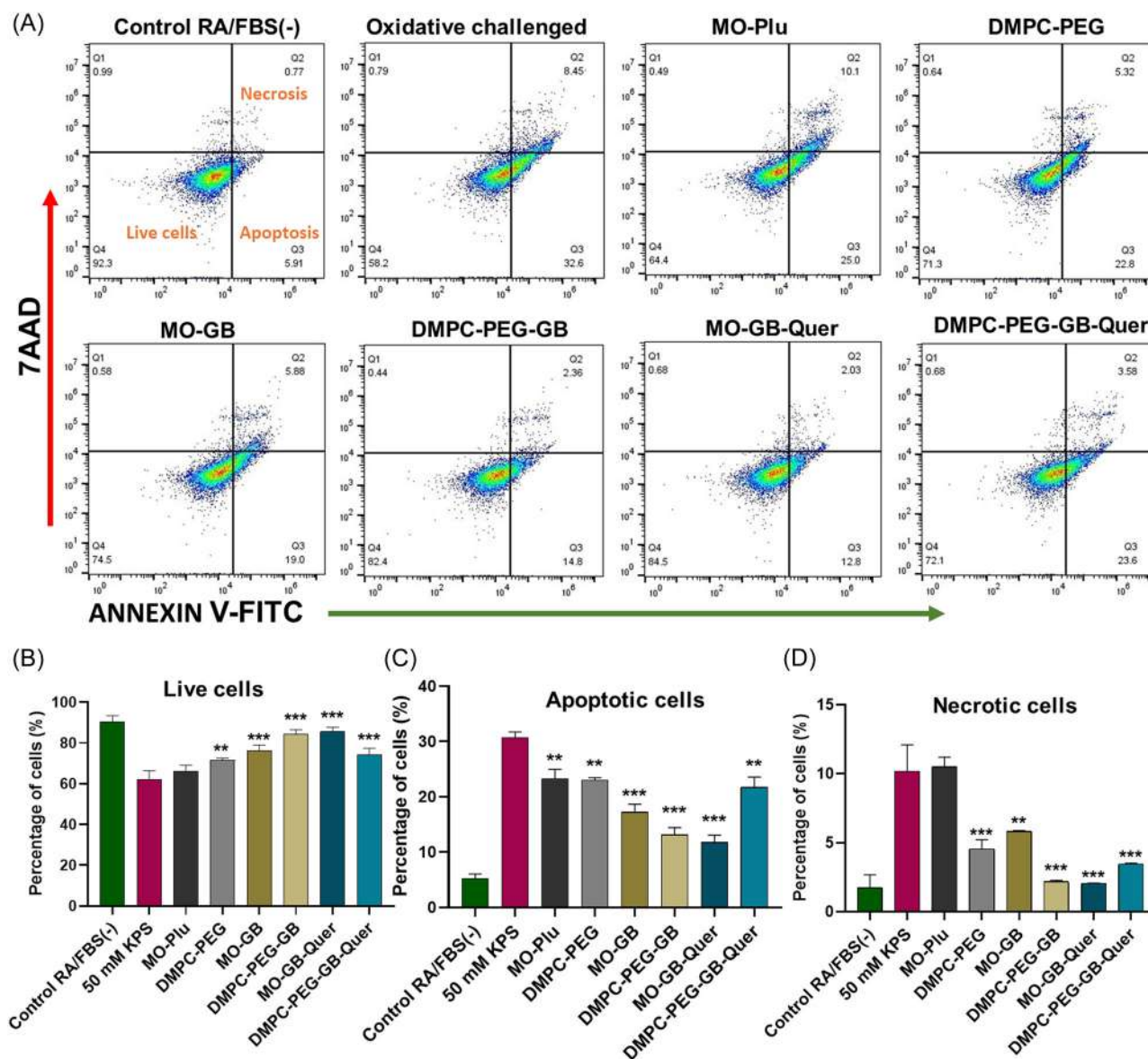


FIGURE 5 Recovery effects of GB-loaded and GB-Quer-loaded LNPs against KPS-induced neuronal cell death determined by apoptosis and necrosis assays using Annexin-V-FITC and PI staining. All groups of SH-SY5Y cells with Annexin-V and PI staining were measured by flow cytometry. (A) Representative dot plots from flow cytometric analysis determining the proportions of live, apoptotic, and necrotic activities. The interpretation of data from quadrant regions in the dot plots is as follows: the bottom left quadrant indicates unstained viable cells with intact membranes, characterized as annexin V-FITC and PI double-negative; the top right quadrant designates necrotic cells identified as annexin V-FITC and PI-positive; and the bottom right quadrant denotes apoptotic cells that are annexin V-FITC-positive but PI-negative. (B–D) The results from flow cytometry analysis are presented in a histogram, showing the mean percentages of live cells (Q4; $n = 3$; $**p = 0.004$, $***p < 0.0001$ for MO-GB, DMPC-PEG-GB and MO-GB-Quer, $***p = 0.0004$ for DMPC-PEG-GB-Quer vs. KPS-treated group) and apoptotic cells (Q3; $n = 3$; $**p = 0.006$, 0.004 and 0.001 for MO-Plu, DMPC-PEG and DMPC-PEG-GB-Quer, $***p < 0.0001$ vs. KPS-treated group). Cells stained with only PI, indicating loss of plasma membrane integrity, were classified as necrotic cells (Q2; $n = 3$; $**p = 0.008$, $***p = 0.0008$ and 0.0002 for DMPC-PEG and DMPC-PEG-GB-Quer, $***p < 0.0001$ for DMPC-PEG-GB and MO-GB-Quer vs. KPS-treated group). The following controls were included: (i) cells exposed to 50 mM KPS [KPS(+)] as a positive control/oxidative-stress challenged; (ii) cells without KPS [KPS(-)] as a negative control; and (iii) untreated cells without annexin V-FITC/PI. Approximately 1.0×10^4 events were recorded and analyzed per individual sample using Flowjo software and one-way analysis of variance (ANOVA). Data is presented as mean \pm SD values of % cells with n representing the number of replicates per group. Statistical differences were calculated using Dunnett's multiple comparison test for one-way ANOVA.

with 1 μ M dose of LNPs (MO-GB, MO-GB-Quer, DMPC-PEG-GB, or DMPC-PEG-GB-Quer) for 24 h significantly protected cells from KPS-induced oxidative stress damage. Pretreatment with cubosomes, loaded with GB or GB/Quer, demonstrated a greater efficacy in

counteracting ROS generation following acute cell exposure to KPS. Figure 6F shows the effect of the studied LNPs in facilitating the recovery of the neuronal cells from oxidative stress induced by KPS. SH-SY5Y cells were exposed to 50 mM KPS for 30 min followed by a

subsequent 24-h treatment with 1 μ M LPNs. The result reveals that direct exposure of cells to 50 mM KPS resulted in a notable increase in ROS levels, quantified by an increased level of DCF staining compared to control cells. The increased DCF intensity was significantly reduced by the GB-loaded LPNs (MO-GB, MO-GB-Quer, DMPC-PEG-GB and DMPC-PEG-GB-Quer) compared to the blank vehicles of MO-Plu and DMPC-PEG, respectively (Figure 6F).

4 | DISCUSSION

Collectively, the investigated here cubosomal and vesicular nano-antioxidants present a promising approach for nanomedicine-mediated ROS downregulation and regeneration from oxidative-stress-related pathologies. The performed study revealed that nanomedicine-mediated treatment with ginkgolide B-loaded

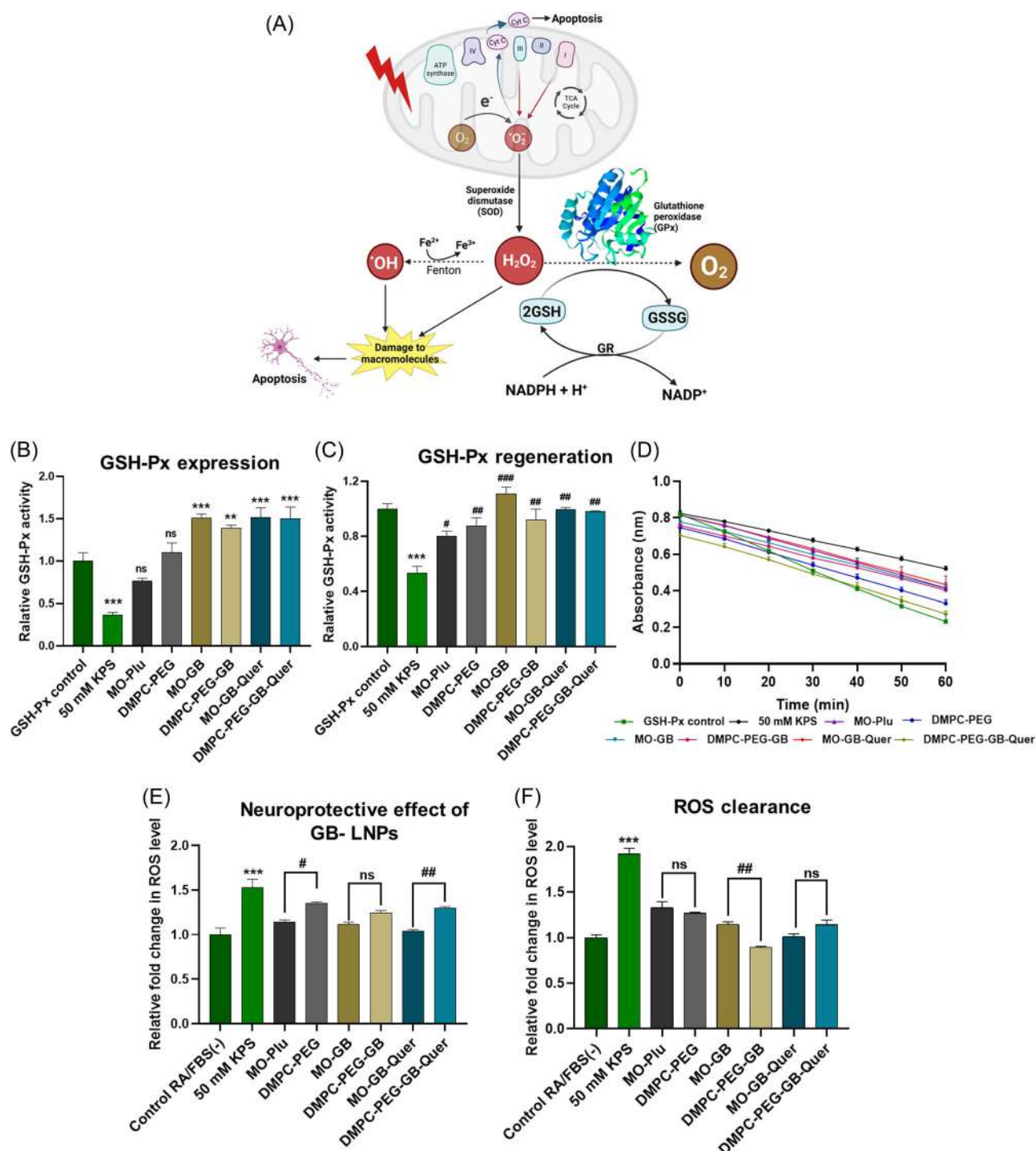


FIGURE 6 (See caption on next page).

cubosomal and vesicular LNPs diminishes intracellular ROS levels through the upregulation of glutathione peroxidase activity.

The SAXS profiles of the MO-based LNPs, encapsulating GB alone or a mixture of GB with quercetin (Quer), exhibited a series of well-discernible Bragg peaks (Figure 3A–C). The q -values of the Bragg peak positions were fitted to that of the first peak (Table S2) to determine the structure of the self-assembled nonlamellar type carriers. The q -vector positions spaced in the ratio $\sqrt{2} : \sqrt{4} : \sqrt{6} : \sqrt{8} : \sqrt{10} : \sqrt{12} : \sqrt{14} : \sqrt{16} \dots$ were assigned to the (110), (200), (211), (220), (310), (222), (321) and (400) reflections of a primitive cubic lattice of the $Im3m$ space group (Q^{IIp}). The corresponding lattice parameters, $a_{(Q)}$, are given in Table 1.

The advantages of the cubic lipid $Im3m$ (Q^{IIp}) nanostructures as drug delivery systems have been emphasized by several studies. For instance, they may enhance the stability and efficacy of therapeutic antioxidant compounds such as GB, quercetin, and curcumin, along with biomolecules like proteins.³¹ The fact that liquid crystalline nanoparticles can be stabilized by Poloxamer surfactants makes them suitable candidates for drug delivery to the brain. *In vivo* studies have shown that MO cubosomes, incorporating a combination of Poloxamer P407 and Tween 80, enhance the delivery of risperidone to the brain via the transnasal route.⁴⁶ The cubosomal formulations have significantly increased drug permeation and brain distribution, indicating that cubosome carriers are suitable for transnasal delivery to the brain.⁴⁶ Liquid crystalline nanoparticles have also been proven effective in the delivery of proteins. For instance, odorranalectin surface-decorated cubosomes encapsulating an anti-Alzheimer S14G-HN peptide, provided enhanced therapeutic effects when administered intranasally.⁴⁷ These formulations also exhibited sustained peptide release, demonstrating the potential of liquid crystalline structures to treat disorders of the CNS.⁴⁷ Recently, cubosome nonlamellar nanoassemblies have shown the ability to modulate

the kinetics of CREB phosphorylation through the AKT/ERK signaling pathway.²⁶

The average values of D_h of the blank nanocarriers (MO-Plu cubosomes and DMPC-PEG vesicles) were around 342 nm and 164 nm, respectively. Two distinct particle populations were observed for the nanocarriers loaded with a single drug (MO-GB and DMPC-PEG-GB) as well as with the co-loaded LNPs (MO-GB-Quer and DMPC-PEG-GB-Quer). The size distributions indicated the coexistence of larger particles (>400 nm) and smaller particles (<200 nm) (Table 1) with a range of polydispersity index (PDI) values resulting from the agitation-dispersion process. The obtained data suggested that the population of the drug-loaded LNPs increases at the expense of the blank nanocarriers. Moreover, hydrophobic drug loading into LNPs enhances the tendency for the formation of larger cubosomes and vesicular particles. Evidently, drug (GB or GB-Quer) loading modifies the hydration level of the lipid membranes which built up the vesicular and cubosomal nanocarriers.

The formulated MO-GB cubosome nanostructure exhibited a slightly higher antioxidant capacity, measured by the Trolox equivalent value (TEAC), compared to the vesicular DMPC-PEG-GB nanostructure. The TEAC values were 281.25 μ M and 251.25 μ M, respectively. The values of TEAC increased upon co-encapsulation of GB and Quer within either cubosomal MO-based (421.5 μ M) or vesicular DMPC nanocarriers (583.07 μ M) (Figure 3C). These results indicated that the co-encapsulation of GB and quercetin within the lipid matrices of MO or DMPC exhibited the highest TAC values of Trolox equivalent and revealed the synergistic effect of the two drug compounds. In the context of neurological long COVID, antioxidants emerge as promising therapeutic agents. They act as anti-inflammatory, antioxidative, and neuroprotective agents by scavenging free radicals and reducing oxidative damage. The synergistic effect between GB and Quer highlights the potential of combination therapies in augmenting antioxidant defenses and addressing oxidative stress-related pathology.

FIGURE 6 Effect of GB-loaded and GB-Quer-loaded LNPs on the regulation of glutathione peroxidase (GSH-Px) enzymatic activity and clearance of ROS in KPS-induced SH-SY5Y model. (A) Schematic representation of GPX-regulated ROS homeostasis. (B) Treatment of differentiated SH-SY5Y cells was performed with LNPs without pre-exposure to KPS. Results are presented as mean \pm SD ($n = 3$, $ns = 0.150$ and 0.847 for MO-Plu and DMPC-PEG, $^{**}p = 0.007$, $^{***}p = 0.0007$ for MO-GB and DMPC-PEG-GB-Quer, $^{***}p = 0.0006$ for MO-GB-Quer vs. GSH-Px control). (C) Incubation with 50 mM KPS for 30 min and subsequent treatment with 1 μ M LNPs for 24 h. Data are reported as mean \pm SD ($n = 2$, $^{***}p = 0.0005$ vs. GSH-Px control, $\#p = 0.038$, $^{##}p = 0.010$, 0.005 , 0.001 , and 0.002 for DMPC-PEG, DMPC-PEG-GB, MO-GB-Quer and DMPC-PEG-GB-Quer, $^{###}p = 0.0003$ vs. KPS treated group). (D) Kinetic change in GSH-Px expression in cells exposed KPS followed by treatment with 1 μ M LNPs for 24 h. n represents the number of replicates per group. Statistical differences were calculated using Dunnett's multiple comparison test for one-way ANOVA. (E,F) Flow cytometric detection of ROS in differentiated SH-SY5Y cells. The fluorescent probe DCFH-DA (10 μ M) was incubated with the cell culture for 30 min. The cells were subjected to varying KPS exposure conditions, pretreatment of differentiated SH-SY5Y cells by nanocarriers loaded with GB or GB and quercetin for 24 h, and determination of intracellular ROS levels under two distinct experimental conditions of exposure to KPS. (E) The cells are first treated with DCFH-DA dye followed by exposure to 50 mM KPS for 5 min before flow cytometry measurements. Data is represented as quantitative histograms of the mean \pm SD values of fluorescence intensity of the DCF dye [DC(+)], expressed as a fold change relative to the background level of untreated cells [RA/FBS(-), DC(+)]. ($n = 2$, $ns = 0.221$ for MO-GB vs. DMPC-PEG-GB, $^{***}p < 0.0001$ vs. control, $\#p = 0.025$ for MO-Plu vs. DMPC-PEG, $^{##}p = 0.008$ for MO-GB-Quer vs. DMPC-PEG-GB-Quer). (F) Exposure of cells to 50 mM KPS for 30 min and subsequent treatment with 1 μ M LNPs during 24 h. This was followed by the incubation of the cells with the DCFH-DA probe for flow cytometry measurements ($n = 2$, $ns = 0.814$ and 0.157 for MO-Plu vs. DMPC-PEG and MO-GB-Quer vs. DMPC-PEG-GB-Quer, $^{***}p < 0.0001$ vs. control group, $^{##}p = 0.004$ for MO-GB vs. DMPC-PEG-GB). n represents the number of replicates per group, with error bars indicating the standard deviation. Statistical differences were calculated using Tukey's multiple comparison test for one-way ANOVA.

It should be noted that antioxidant activity, assessed through different *in vitro* assays (DPPH or CUPRAC), may yield varied results due to the distinct mechanisms (reducing/scavenging action) and principles of these assays. In the present study, a good correlation was established between the results obtained through the DPPH and CUPRAC methods.

The *in vitro* cellular studies demonstrates that KPS induces oxidative stress by affecting the production of ROS (such as H_2O_2) accompanied by the depletion of glutathione peroxidase function, altered dopamine metabolism, and triggered both necrotic and apoptotic cell death pathways. These findings are in accordance with other studies, which employed 6-OHDA- or MPTP-induced oxidative stress to damage neuronally-derived SH-SY5Y cells.^{13,48} Furthermore, in comparison to 2,2'-azobis(2-amidinopropane) dihydrochloride (AAPH) in an ORAC assay, KPS was found to be a moderate ROS generator (Figure S1).

Apoptosis is influenced by multiple factors that can either promote cell survival or induce programmed cell death. Notably, elevated ROS levels can trigger mitochondrial dysfunction, leading to the release of apoptosis inducers. Proapoptotic proteins (Bax and Bad) and antiapoptotic proteins (Bcl-2 and Bcl-XL) complement each other to regulate cell survival/death.

The neuroprotective effect of EGb was validated in previous *in vitro* and *in vivo* model studies. *In vitro* studies have revealed that EGb protects cultured neurons against cell death induced by H_2O_2 and MPTP.^{49–53} Moreover, *Ginkgo biloba* (EGb761) and its extracts (quercetin and GB) can protect SH-SY5Y cells against A β -induced neurotoxicity by obstructing A β -induced events, such as glucose uptake, ROS accumulation, mitochondrial dysfunction, and activation of protein kinase B (AKT). These compounds regulate also the transcription of inducible antioxidant elements, paraoxonase-2 (PON2), a calcium-dependent lactonase with antioxidant functions, c-Jun N-terminal kinases (JNK) and extracellular signal-regulated kinases (ERK 1/2) pathways, which participate in inflammatory and apoptotic signaling pathways.^{54–56}

Oxidative-stress trigger, experienced in severe COVID, is regarded as one of the main factors of neuronal damage, causing neurodegenerative as well as depressive and anxiolytic disorders.⁵⁷ Quercetin has been discussed in a few recent studies, including an open-label clinical study, showing good tolerability and benefits in preventing the severe outcomes of the coronavirus infection disease.^{58,59} The free drug combination of quercetin and GB has exhibited neuroprotective effects against oxidative stress synergistically via decreasing malondialdehyde (MDA) content and increasing the levels of antioxidant enzymes, SOD, GSH, and CAT.^{13,14,60} Furthermore, nanocarriers loaded with EGb extracts of GB and quercetin could modulate antioxidative signaling pathways, such as the nuclear factor (erythroid-derived 2)-like 2 (Nrf2). The neuroprotective effect of GB, delivered via biodegradable poly(ethylene glycol)-b-poly(trimethylene carbonate) (PEG-PTMC) nanoparticles (PPNPs), has been explored as a promising therapy for PD to enhance its accumulation in the blood and brain.¹³

GB-PPNPs were able to facilitate sustained GB release during 48 h, thus protecting against MPP⁺-induced neuronal cytotoxicity. GB-loaded NPs (GB-PPNPs) have been shown to improve locomotor activity, dopamine and its metabolite levels, and tyrosine hydroxylase activity in an animal model of Parkinson's disease.¹³

Our results support the hypothesis that EGb exerts significant antiapoptotic and neuroprotective effects, which are likely mediated by the ability to neutralize harmful free radicals. We show that this activity is essentially enhanced when EGb ingredients are delivered via lipid nanocarrier systems. Regarding the role of the nanostructural organization, the direct comparison of the studied nanostructures, namely GB-loaded and GB-quercetin co-loaded cubosomes or GB-loaded and GB-quercetin co-loaded DMPC vesicles, in the same experimental setting, revealed quantitatively different hydroxyl radical-scavenging activities. The *in vitro* established pharmacological properties, which include a reduction in neuronal apoptosis and necrosis induced by KPS, present interest for the application of these nanocarriers in potential recovery from neuronal damages provoked by oxidative stress.

We observed a statistically significant enhancement in GSH-Px activity in SH-SY5Y cells treated with GB-loaded cubosomes (MO-GB) compared to DMPC-PEG-GB vesicles. Additionally, co-encapsulation of GB/Quer within the MO cubosome nanocarrier further increased GSH-Px activity. These results suggest that the reduction in ROS levels may have contributed to the enhancement of GSH-Px activity. Therefore, the decrease in ROS levels facilitated by the LNPs could potentially alleviate oxidative stress conditions, consequently leading to an increase in GSH-Px activity (Figure 7).

In a recent study, it has been reported that GB nano-therapy has a protective effect on MTPT-induced PD mice model. The striatal GSH-Px levels were upregulated up to 94.86 ± 9.15 U/mg protein relative to the MPTP mice model (63.92 ± 6.06 U/mg protein). This indicated the significant role of nanoparticles in facilitating the delivery of therapeutic agents across the BBB.⁵²

The co-encapsulation of GB and Quer within the MO cubosome nanocarriers exhibited a greater efficacy in attenuating ROS generation compared to the individual drug GB. In comparison, GB encapsulation in DMPC vesicles resulted in a lower ROS scavenging activity compared to the dual-loaded nanoformulation (DMPC-PEG-GB-Quer).

We considered that the variation in fluorescence intensity observed between the LNPs of the nonlamellar lipid MO or the lamellar phospholipid DMPC can be due to the different compositions of these systems determining their internal liquid crystalline structure.²⁷ We also considered that the type and the concentration of the employed dispersing agent may affect the LNP structure type, thus influencing the incorporation of antioxidants in the lipid formulations.^{61–64} Regarding the employed stabilizing surfactants, the MO-GB-Quer and DMPC-PEG-GB LNPs, dispersed by Pluronic F127 and the DOPE-PEG₂₀₀₀, exhibited strong reduction in ROS. Therefore, we can correlate the findings of this study, which indicate that encapsulating GB in the phospholipid DMPC bilayer and

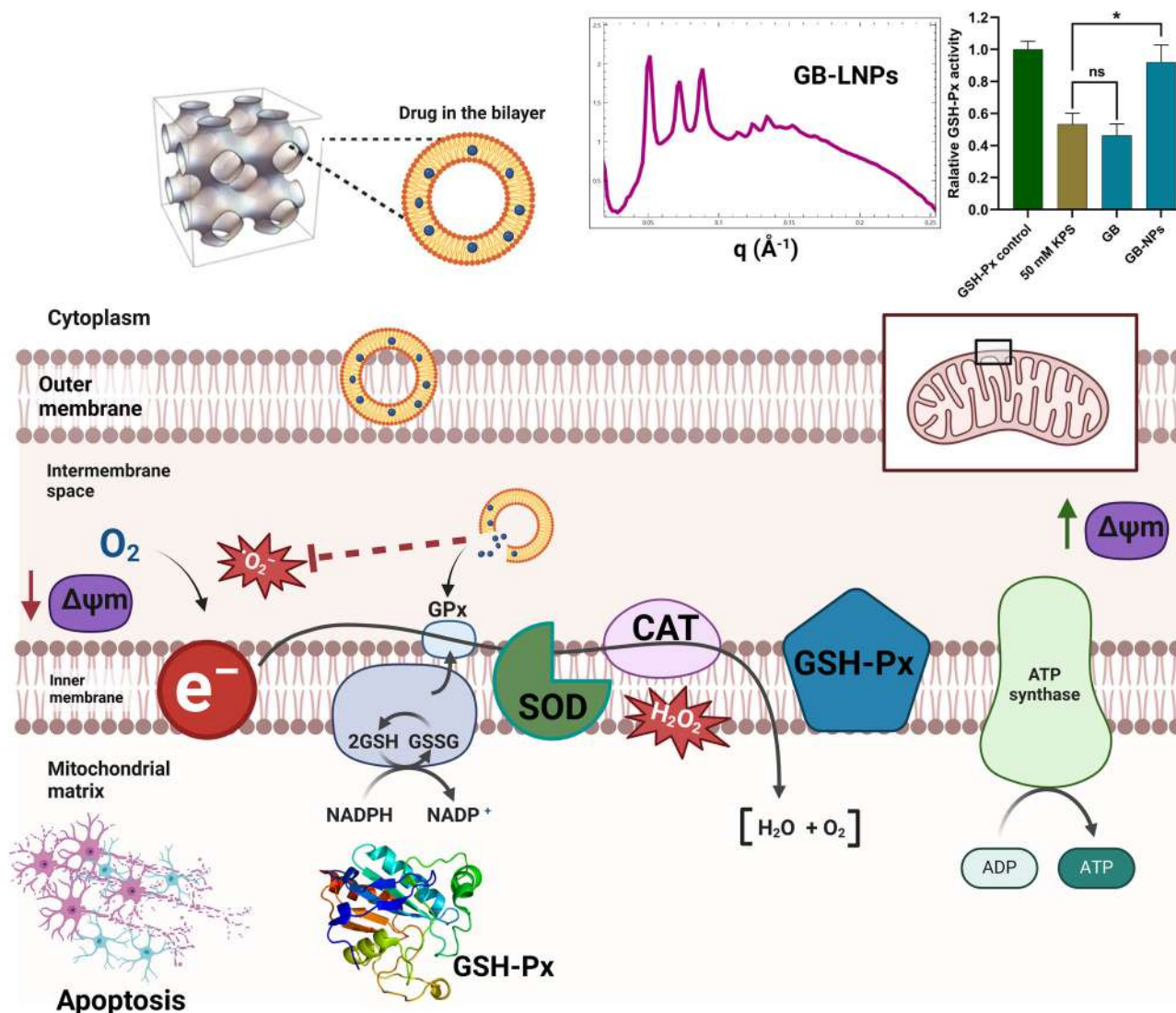


FIGURE 7 GB-LNPs are suggested to exert neuroprotective effects by scavenging free radicals and enhancing antioxidant systems such as CAT, SOD, and GSH-Px to maintain redox homeostasis.

simultaneously co-encapsulating GB/Quer in the MO lipid matrix reduces ROS levels significantly. These findings may also be explained by other factors, such as nanoparticle supramolecular architectures, which affect the bioactive compounds' release mechanisms.

5 | CONCLUSION

In the present study, we successfully developed lipid-based liquid crystalline nanostructures of cubosome and vesicle LNP types to co-encapsulate and deliver neuroprotective antioxidant molecules (ginkgolide B (GB) and quercetin). These LNPs enabled the inhibition of ROS production and neuronal apoptosis. A novel experimental model of KPS-induced oxidative damage, likely associated with transient neuronal damage, was proposed and validated. The structural characterization of MO-based LNPs, encapsulating ginkgolide B alone or in combination with quercetin, revealed well-

discernible Bragg peaks indicative of a primitive cubic lattice structure. These cubic lipid *Im3m* (QIIP) nanostructures offer advantages for drug delivery, enhancing the stability and efficacy of therapeutic antioxidant compounds such as ginkgolide B and quercetin. The in vitro results with differentiated SH-SY5Y cells demonstrated that GB-loaded LNPs exhibit enhanced neuroprotective effects, mediated by their ability to neutralize harmful free radicals, and upregulates glutathione peroxidase levels to maintain redox homeostasis. The nanosystems exhibited different effects in scavenging free radicals due to their unique nanostructure.

Furthermore, the developed cubosomal and vesicular lipid-based nanocarriers showed potent antioxidant and antiapoptotic activities in the created KPS-induced oxidative stress model. Thus, they offer a potential new therapeutic approach for the management of neurological complications associated with long COVID/post-acute COVID conditions and other neurological complications provoked by oxidative stress. Our study establishes a correlation between nanomedicine-mediated

ROS reduction and the enhancement of glutathione peroxidase activity, suggesting a potential mechanism for alleviating oxidative stress conditions. Therefore, future research is needed to understand the mechanisms of GB-LNPs on other signaling pathways, such as inflammatory pathways, which are highly triggered during severe COVID conditions. Further work would be required to translate these nanosystems into clinical applications for the treatment of neurodegenerative conditions including Alzheimer's and Parkinson's diseases.

AUTHOR CONTRIBUTIONS

Conceptualization, design, planning, and management: Angelina Angelova Experimental design, planning, performance, and data acquisition: Thelma Akanchise and Angelina Angelova Data analysis and interpretation: Thelma Akanchise, Angelina Angelova, and Borislav Angelov Writing, reviewing, and revising the manuscript: Thelma Akanchise, Angelina Angelova, and Borislav Angelov All authors critically reviewed the manuscript and approved the final manuscript for submission.

ACKNOWLEDGMENTS

Thelma Akanchise acknowledges a PhD fellowship from Campus France, and Angelina Angelova acknowledges membership in the CNRS GDR2088 BIOMIM research network. Figures 1, 6A, and 7 were generated with [BioRender.com](https://www.biorender.com) (accessed on October 6, 2023). The performed research was funded by the projects "Structural Dynamics of Biomolecular Systems" (ELIBIO) (CZ.02.1.01/0.0/0.0/15_003/0000447) and "Advanced research using high-intensity laser produced photons and particles" (CZ.02.1.01/0.0/0.0/16_019/0000789) from the European Regional Development Fund. The authors acknowledge the scientific support by Dr. Thomas Bizien at the SWING beamline of Synchrotron SOLEIL (Saint Aubin, France) and the allocation of beam time through the projects 20210580 and 20230326. Thelma Akanchise thanks Dr. Juliette Vergnaud and Mélanie Hery for helpful advice at the cell culture facility.

CONFLICT OF INTEREST STATEMENT

The authors declare no conflict of interest.

DATA AVAILABILITY STATEMENT

The data that support the findings of this study are available from the corresponding author upon reasonable request. All data, materials, and methods are included in the article.

ORCID

Angelina Angelova  <http://orcid.org/0000-0002-0285-0637>

REFERENCES

- Varachalam SP, Lahooti B, Chamaneh M, et al. Nanomedicine for the SARS-CoV-2: state-of-the-art and future prospects. *Int J Nanomedicine*. 2021;16:539-560. doi:10.2147/IJN.S283686
- Hald Albertsen C, Kulkarni JA, Witzigmann D, Lind M, Petersson K, Simonsen JB. The role of lipid components in lipid nanoparticles for vaccines and gene therapy. *Adv Drug Deliv Rev*. 2022;188:114416. doi:10.1016/j.addr.2022.114416
- Mainardes RM, Diedrich C. The potential role of nanomedicine on COVID-19 therapeutics. *Ther Delivery*. 2020;11(7):411-414. doi:10.4155/tde-2020-0069
- Premraj L, Kannapadi NV, Briggs J, et al. Mid and long-term neurological and neuropsychiatric manifestations of post-COVID-19 syndrome: a meta-analysis. *J Neurol Sci*. 2022;434:120162. doi:10.1016/j.jns.2022.120162
- Harapan BN, Yoo HJ. Neurological symptoms, manifestations, and complications associated with severe acute respiratory syndrome coronavirus 2 (SARS-CoV-2) and coronavirus disease 19 (COVID-19). *J Neurol*. 2021;268(9):3059-3071. doi:10.1007/s00415-021-10406-y
- Carfi A, Bernabei R, Landi F, for the Gemelli Against COVID-19 Post-Acute Care Study Group. Persistent symptoms in patients after acute COVID-19. *JAMA*. 2020;324(6):603. doi:10.1001/jama.2020.12603
- Delgado-Roche L, Mesta F. Oxidative stress as key player in severe acute respiratory syndrome coronavirus (SARS-CoV) infection. *Arch Med Res*. 2020;51(5):384-387. doi:10.1016/j.arcmed.2020.04.019
- Nuzzo D, Cambula G, Bacile I, et al. Long-term brain disorders in Post Covid-19 Neurological Syndrome (PCNS) patient. *Brain Sci*. 2021;11(4):454. doi:10.3390/brainsci11040454
- Boroujeni ME, Simani L, Bluysen HAR, et al. Inflammatory response leads to neuronal death in human post-mortem cerebral cortex in patients with COVID-19. *ACS Chem Neurosci*. 2021;12(12):2143-2150. doi:10.1021/acscchemneuro.1c00111
- Nuzzo D, Picone P. Potential neurological effects of severe COVID-19 infection. *Neurosci Res*. 2020;158:1-5. doi:10.1016/j.neures.2020.06.009
- Nair A, Sharma P, Tiwary M. Glutathione deficiency in COVID19 illness-does supplementation help? *Saudi J Anaesth*. 2021;15(4):458. doi:10.4103/sja.sja_320_21
- Djanaguiraman M, Boyle DL, Welti R, Jagadish SVK, Prasad PVV. Decreased photosynthetic rate under high temperature in wheat is due to lipid desaturation, oxidation, acylation, and damage of organelles. *BMC Plant Biol*. 2018;18(1):55. doi:10.1186/s12870-018-1263-z
- Wang Q, Ma R, Liu P, et al. Efficient sustained-release nanoparticle delivery system protects nigral neurons in a toxin model of Parkinson's disease. *Pharmaceutics*. 2022;14(8):1731. doi:10.3390/pharmaceutics14081731
- Akanchise T, Angelova A. *Ginkgo biloba* and Long COVID: in vivo and in vitro models for the evaluation of nanotherapeutic efficacy. *Pharmaceutics*. 2023;15(5):1562. doi:10.3390/pharmaceutics15051562
- Angelova A, Angelov B, Drechsler M, Bizien T, Gorshkova YE, Deng Y. Plasmalogen-Based liquid crystalline multiphase structures involving docosapentaenoyl derivatives inspired by biological cubic membranes. *Front Cell Dev Biol*. 2021;9:617984. doi:10.3389/fcell.2021.617984
- De Torre MP, Cavero RY, Calvo MI, Vizmanos JL. A simple and a reliable method to quantify antioxidant activity in vivo. *Antioxidants*. 2019;8(5):142. doi:10.3390/antiox8050142
- Rolnik A, Soluch A, Kowalska I, Olas B. Antioxidant and hemostatic properties of preparations from Asteraceae family and their chemical composition—comparative studies. *Biomed Pharmacother*. 2021;142:111982. doi:10.1016/j.biopha.2021.111982
- Kamiloglu S, Sari G, Ozdal T, Capanoglu E. Guidelines for cell viability assays. *Food Frontiers*. 2020;1(3):332-349. doi:10.1002/fft2.44
- Rakotoarisoa M, Angelov B, Espinoza S, Khakurel K, Bizien T, Angelova A. Cubic liquid crystalline nanostructures involving catalase and curcumin: BioSAXS study and catalase peroxidatic function after cubosomal nanoparticle treatment of differentiated SH-SY5Y cells. *Molecules*. 2019;24(17):3058. doi:10.3390/molecules24173058

20. Kim H, Xue X. Detection of total reactive oxygen species in adherent cells by 2',7'-Dichlorodihydrofluorescein diacetate staining. *JoVE*. 2020;160:60682. doi:10.3791/60682
21. Cossarizza A, Ferraresi R, Troiano L, et al. Simultaneous analysis of reactive oxygen species and reduced glutathione content in living cells by polychromatic flow cytometry. *Nat Protoc*. 2009;4(12):1790-1797. doi:10.1038/nprot.2009.189
22. Amiri F, Dahaj MM, Siasi NH, Deyhim MR. Treatment of platelet concentrates with the L-carnitine modulates platelets oxidative stress and platelet apoptosis due to mitochondrial reactive oxygen species reduction and reducing cytochrome C release during storage. *J Thromb Thrombolysis*. 2021;51(2):277-285. doi:10.1007/s11239-020-02241-1
23. Arazi H, Mohammadjafari H, Asadi A. Use of anabolic androgenic steroids produces greater oxidative stress responses to resistance exercise in strength-trained men. *Toxicol Rep*. 2017;4:282-286. doi:10.1016/j.toxrep.2017.05.005
24. Sullivan-Gunn MJ, Campbell-O'sullivan SP, Tisdale MJ, Lewandowski PA. Decreased NADPH oxidase expression and antioxidant activity in cachectic skeletal muscle. *J Cachexia Sarcopenia Muscle*. 2011;2(3):181-188. doi:10.1007/s13539-011-0037-3
25. Dhall S, Do DC, Garcia M, et al. Generating and reversing chronic wounds in diabetic mice by manipulating wound redox parameters. *J Diabetes Res*. 2014;2014:1-18. doi:10.1155/2014/562625
26. Wu Y, Angelov B, Deng Y, et al. Sustained CREB phosphorylation by lipid-peptide liquid crystalline nanoassemblies. *Commun Chem*. 2023;6(1):241. doi:10.1038/s42004-023-01043-9
27. Rakotoarisoa M, Angelov B, Garamus VM, Angelova A. Curcumin and fish oil-loaded spongosome and cubosome nanoparticles with neuroprotective potential against H₂O₂-induced oxidative stress in differentiated human SH-SY5Y cells. *ACS Omega*. 2019;4(2):3061-3073. doi:10.1021/acsomega.8b03101
28. Esposito E, Sguizzato M, Drechsler M, et al. Lipid nanostructures for antioxidant delivery: a comparative preformulation study. *Beilstein J Nanotechnol*. 2019;10:1789-1801. doi:10.3762/bjnano.10.174
29. Kulkarni CV, Wachter W, Iglesias-Salto G, Engelskirchen S, Ahualli S. Monoolein: a magic lipid? *Phys Chem Chem Phys*. 2011;13(8):3004-3021. doi:10.1039/C0CP01539C
30. Bouffieux O, Berquand A, Eeman M, et al. Molecular organization of surfactin-phospholipid monolayers: effect of phospholipid chain length and polar head. *Biochimica et Biophysica Acta (BBA) - Biomembranes*. 2007;1768(7):1758-1768. doi:10.1016/j.bbame.2007.04.015
31. Sivadason D, Sultan MH, Alqahtani SS, Javed S. Cubosomes in drug delivery—a comprehensive review on its structural components, preparation techniques and therapeutic applications. *Biomedicine*. 2023;11(4):1114. doi:10.3390/biomedicine11041114
32. Angelova A, Drechsler M, Garamus VM, Angelov B. Pep-lipid cubosomes and vesicles compartmentalized by Micelles from self-assembly of multiple neuroprotective building blocks including a large peptide hormone PACAP-DHA. *ChemNanoMat*. 2019;5(11):1381-1389. doi:10.1002/cnma.201900468
33. Rakotoarisoa M, Angelov B, Espinoza S, et al. Composition-switchable liquid crystalline nanostructures as green formulations of curcumin and fish oil. *ACS Sustain Chem Eng*. 2021;9(44):14821-14835. doi:10.1021/acssuschemeng.1c04706
34. Fracassi A, Podolsky KA, Pandey S, et al. Characterizing the self-assembly properties of monoolein lipid isosteres. *J Phys Chem B*. 2023;127(8):1771-1779. doi:10.1021/acs.jpcc.2c07215
35. Zengin G, Aktumsek A. Investigation of antioxidant potentials of solvent extracts from different anatomical parts of *Asphodeline Anatolica* E. tuzlaci: an endemic plant to Turkey. *Afr J Tradit Complement Altern Med*. 2014;11(2):481. doi:10.4314/ajtcam.v11i2.37
36. Circu ML, Aw TY. Reactive oxygen species, cellular redox systems, and apoptosis. *Free Radic Biol Med*. 2010;48(6):749-762. doi:10.1016/j.freeradbiomed.2009.12.022
37. Ferreira CA, Ni D, Rosenkrans ZT, Cai W. Scavenging of reactive oxygen and nitrogen species with nanomaterials. *Nano Res*. 2018;11(10):4955-4984. doi:10.1007/s12274-018-2092-y
38. Sies H, Berndt C, Jones DP. Oxidative stress. *Annu Rev Biochem*. 2017;86(1):715-748. doi:10.1146/annurev-biochem-061516-045037
39. Di Meo S, Reed TT, Venditti P, Victor VM. Role of ROS and RNS sources in physiological and pathological conditions. *Oxid Med Cell Longevity*. 2016;2016:1-44. doi:10.1155/2016/1245049
40. Navarro-Yepes J, Zavala-Flores L, Anandhan A, et al. Antioxidant gene therapy against neuronal cell death. *Pharmacol Ther*. 2014;142(2):206-230. doi:10.1016/j.pharmthera.2013.12.007
41. Sies H, Jones DP. Reactive oxygen species (ROS) as pleiotropic physiological signalling agents. *Nat Rev Mol Cell Biol*. 2020;21(7):363-383. doi:10.1038/s41580-020-0230-3
42. Aranda-Rivera AK, Cruz-Gregorio A, Arancibia-Hernández YL, Hernández-Cruz EY, Pedraza-Chaverri J. RONS and oxidative stress: an overview of basic concepts. *Oxygen*. 2022;2(4):437-478. doi:10.3390/oxygen2040030
43. Popa-Wagner A, Mitran S, Sivanesan S, Chang E, Buga AM. ROS and brain diseases: the good, the bad, and the ugly. *Oxid Med Cell Longevity*. 2013;2013:1-14. doi:10.1155/2013/963520
44. Sharifi-Rad J, Rapposelli S, Sestito S, et al. Multi-target mechanisms of phytochemicals in Alzheimer's disease: effects on oxidative stress, neuroinflammation and protein aggregation. *J Pers Med*. 2022;12(9):1515. doi:10.3390/jpm12091515
45. Lee Mosley R, Benner EJ, Kadiu I, et al. Neuroinflammation, oxidative stress, and the pathogenesis of Parkinson's disease. *Clin Neurosci Res*. 2006;6(5):261-281. doi:10.1016/j.cnr.2006.09.006
46. Abdelrahman FE, Elsayed I, Gad MK, Badr A, Mohamed MI. Investigating the cubosomal ability for transnasal brain targeting: in vitro optimization, ex vivo permeation and in vivo biodistribution. *Int J Pharm*. 2015;490(1-2):281-291. doi:10.1016/j.ijpharm.2015.05.064
47. Wu H, Li J, Zhang Q, et al. A novel small Odorranalectin-bearing cubosomes: preparation, brain delivery and pharmacodynamic study on amyloid-β25-35-treated rats following intranasal administration. *Eur J Pharmaceut Biopharmaceut*. 2012;80(2):368-378. doi:10.1016/j.ejpb.2011.10.012
48. Cirmi S, Maugeri A, Lombardo GE, et al. A flavonoid-rich extract of mandarin juice counteracts 6-OHDA-induced oxidative stress in SH-SY5Y cells and modulates Parkinson-related genes. *Antioxidants*. 2021;10(4):539. doi:10.3390/antiox10040539
49. Oyama Y, Chikahisa L, Ueha T, Kanemaru K, Noda K. *Ginkgo biloba* extract protects brain neurons against oxidative stress induced by hydrogen peroxide. *Brain Res*. 1996;712(2):349-352. doi:10.1016/0006-8993(95)01440-3
50. Chen C, Wei T, Gao Z, et al. Different effects of the constituents of EGB761 on apoptosis in rat cerebellar granule cells induced by hydroxyl radicals. *IUBMB Life*. 1999;47(3):397-405. doi:10.1080/15216549900201423
51. Xin W, Wei T, Chen C, Ni Y, Zhao B, Hou J. Mechanisms of apoptosis in rat cerebellar granule cells induced by hydroxyl radicals and the effects of EGB761 and its constituents. *Toxicology*. 2000;148(2-3):103-110. doi:10.1016/S0300-483X(00)00200-6
52. Guidetti C, Paracchini S, Lucchini S, Cambieri M, Marzatico F. Prevention of neuronal cell damage induced by oxidative stress in vitro: effect of different *Ginkgo biloba* extracts. *J Pharm Pharmacol*. 2010;53(3):387-392. doi:10.1211/0022357011775442
53. Yang SF, Wu Q, Sun AS, Huang XN, Shi JS. Protective effect and mechanism of *Ginkgo biloba* leaf extracts for Parkinson disease induced by 1-methyl-4-phenyl-1,2,3,6-tetrahydropyridine. *Acta Pharmacol Sin*. 2001;22(12):1089-1093.

54. Alvarez-Arellano L, Salazar-García M, Corona JC. Neuroprotective effects of quercetin in pediatric neurological diseases. *Molecules*. 2020;25(23):5597. doi:10.3390/molecules25235597
55. Schroeter H, Spencer JPE, Rice-Evans C, Williams RJ. Flavonoids protect neurons from oxidized low-density-lipoprotein-induced apoptosis involving c-Jun N-terminal kinase (JNK), c-Jun and caspase-3. *Biochem J*. 2001;358(3):547-557. doi:10.1042/bj3580547
56. Shi C, Zhao L, Zhu B, et al. Protective effects of *Ginkgo biloba* extract (EGb761) and its constituents quercetin and ginkgolide B against β -amyloid peptide-induced toxicity in SH-SY5Y cells. *Chemico-Biol Interact*. 2009;181(1):115-123. doi:10.1016/j.cbi.2009.05.010
57. Merzoug S, Toumi ML, Tahraoui A. Quercetin mitigates Adriamycin-induced anxiety- and depression-like behaviors, immune dysfunction, and brain oxidative stress in rats. *Naunyn-Schmiedeberg's Arch Pharmacol*. 2014;387(10):921-933. doi:10.1007/s00210-014-1008-y
58. Di Pierro F, Derosa G, Maffioli P, et al. Possible therapeutic effects of adjuvant quercetin supplementation against early-stage COVID-19 infection: a prospective, randomized, controlled, and open-label study. *Int J Gen Med*. 2021;14:2359-2366. doi:10.2147/IJGM.S318720
59. Derosa G, Maffioli P, D'Angelo A, Di Pierro F. A role for quercetin in coronavirus disease 2019 (COVID-19). *Phytother Res*. 2021;35(3):1230-1236. doi:10.1002/ptr.6887
60. Achete de Souza G, de Marqui SV, Matias JN, Guiguer EL, Barbalho SM. Effects of *Ginkgo biloba* on diseases related to oxidative stress. *Planta Med*. 2020;86(06):376-386. doi:10.1055/a-1109-3405
61. Domingues RB, Mendes-Correa MC, de Moura Leite FBV, et al. First case of SARS-COV-2 sequencing in cerebrospinal fluid of a patient with suspected demyelinating disease. *J Neurol*. 2020;267(11):3154-3156. doi:10.1007/s00415-020-09996-w
62. Vollbracht C, Kraft K. Oxidative stress and hyper-inflammation as major drivers of severe COVID-19 and long COVID: implications for the benefit of high-dose intravenous vitamin C. *Front Pharmacol*. 2022;13:899198. doi:10.3389/fphar.2022.899198
63. Ekambaram P, Abdul Hasan Sathali A. Formulation and evaluation of solid lipid nanoparticles of Ramipril. *J Young Pharmacist*. 2011;3(3):216-220. doi:10.4103/0975-1483.83765
64. Bonaccorso A, Pellitteri R, Ruozzi B, et al. Curcumin loaded polymeric vs. lipid nanoparticles: antioxidant effect on normal and hypoxic olfactory ensheathing cells. *Nanomaterials*. 2021;11(1):159. doi:10.3390/nano11010159

SUPPORTING INFORMATION

Additional supporting information can be found online in the Supporting Information section at the end of this article.

How to cite this article: Akanchise T, Angelov B, Angelova A. Nanomedicine-mediated recovery of antioxidant glutathione peroxidase activity after oxidative-stress cellular damage: insights for neurological long COVID. *J Med Virol*. 2024;96:e29680. doi:10.1002/jmv.29680